Gas Electron Multipliers and a Scanner for Automated Quality Control

by

Brian Paul Tamm

Submitted to the Department of Physics
in partial fulfillment of the requirements for the degree of

Bachelor of Science in Physics

at the

MASSACHUSETTS INSTITUTE OF TECHNOLOGY

May 2005 [June 2005]

Author .....
Department of Physics
May 11, 2005

Certified by .....
Ulrich J. Becker
Professor, Department of Physics
Thesis Supervisor

Accepted by .....
Professor David E. Pritchard
Senior Thesis Coordinator, Department of Physics

Gas Electron Multipliers and a Scanner for Automated Quality Control

by

Brian Paul Tamm

Submitted to the Department of Physics
on May 11, 2005, in partial fulfillment of the
requirements for the degree of
Bachelor of Science in Physics

Abstract

The gas electron multiplier (GEM) is a novel charge amplification element for use in gaseous particle detectors. Because of their high gain ($\sim 10^5$ when cascaded) and ability to withstand harsh radiation conditions, GEMs have been selected for use in the time projection chambers of the latest high-energy experiments, including COMPASS, STAR, and the planned ILC. Foil quality has been found to be critical for optimal GEM performance. If an irregularity in just one of the roughly 600,000 amplification holes of a 10×10 cm GEM induces a spark discharge, the entire GEM is useless. Computer simulations have also shown that amplification behavior is strongly dependent on hole diameter and shape. To improve foil quality control, an automated scanner has been constructed to optically examine every hole in a GEM. The machine can measure each hole's outer copper diameter and inner Kapton diameter and locate and geometrically classify any foil imperfections. The scanner has been used to characterize GEMs recently manufactured by Tech-Etch. These scans indicate a general absence of etching defects, but measured diameter inhomogeneity may result in gain variations as large as $\pm 20\%$ over the active foil area.

Thesis Supervisor: Ulrich J. Becker
Title: Professor, Department of Physics

Acknowledgments

I would like to thank my thesis adviser Professor Ulrich Becker, lab technician Scott Hertel, machinist Michael Grossman, and all the students of the Building 44 Gas R&D Lab. This thesis could not have been completed without their expertise, guidance, and support.

Contents

List of Figures

List of Tables

Chapter 1

Motivation

This chapter provides an overview of the gas electron multiplier (GEM), its current role in high-energy physics experiments, the problem of producing consistent high quality GEMs, and the need to implement automated quality control.

1.1 Overview of the GEM

GEMs were first developed in the mid-1990's by Fabio Sauli at CERN [1]. A GEM is a laminate foil product consisting of a dielectric sheet clad on both sides with a thin layer of copper. The copper-clad sheet is photo-lithographically etched on both sides to create a high-density array of holes. Dielectric thicknesses of 50 μm, copper thicknesses of 5 μm, and hole diameters and spacings of order 100 μm are typical. An image of one of the early GEMs produced at CERN is shown in Figure 1-1.

When a high voltage (on the order of hundreds of volts) is applied between the copper layers, an enormous electric field (on the order of 10^5 V/cm) develops within the holes. Placed within a gaseous particle detector, the GEM can serve as a highly effective charge amplification element. Details of GEM electrostatics and amplification are addressed in Chapter 3.

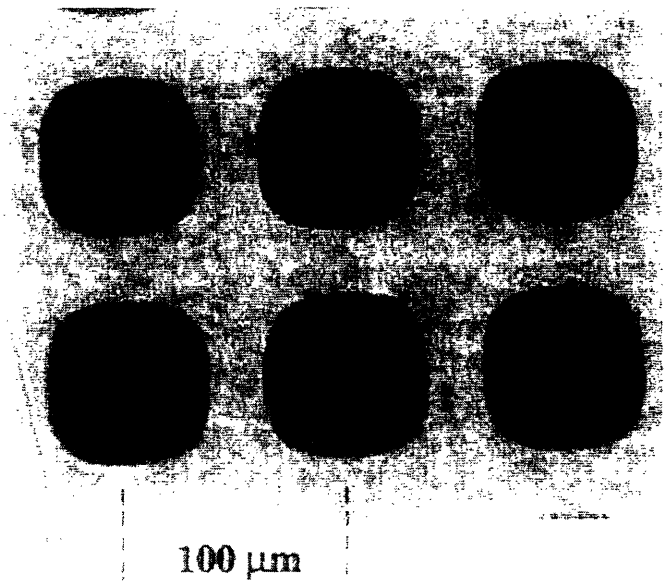

Figure 1-1: Microphotograph of early CERN GEM. Image reproduced from Ref. [1].

1.2 Physics Applications of GEMs

The use of GEM-based detectors is enabling the exploration of several new realms of physics. The goal of this section is both to present a brief description of this physics and to motivate the need to produce large numbers of high-quality GEMs. The COMPASS and STAR experiments as well as the planned International Linear Collider are discussed. GEMs have also generated interest outside the high-energy physics community. Section 1.2.4 describes the use of GEMs for medical and astronomical x-ray imaging.

1.2.1 COMPASS

The COmmon Muon and Proton Apparatus for Structure and Spectroscopy (COMPASS) [2] is a new experiment at CERN studying collisions between high-energy muons and fixed target nuclei

$$\mu + A \rightarrow \mu' + X\,. \tag{1.1}$$

The experiment uses a high-intensity beam of muons at 160 GeV/c from CERN's Super Proton Synchrotron (SPS) to probe the quark-gluon structure of nucleons. It also hopes to solve the mystery of how three spin-1/2 quarks and numerous spin-1 gluons combine to form nucleons known to have spin-1/2 at all times [3].

The experimental apparatus (shown schematically in Figure 1-2) includes 20 large (31×31 cm) triple GEM detectors positioned normal to the beam [4, 5]. These detectors are used both to measure the profile of the muon beam and to track protons (or mesons) produced in the near-beam (small-angle) region. As the first large experiment to rely entirely on GEMs for tracking in this region, COMPASS also serves as a proof of concept for this new technology.

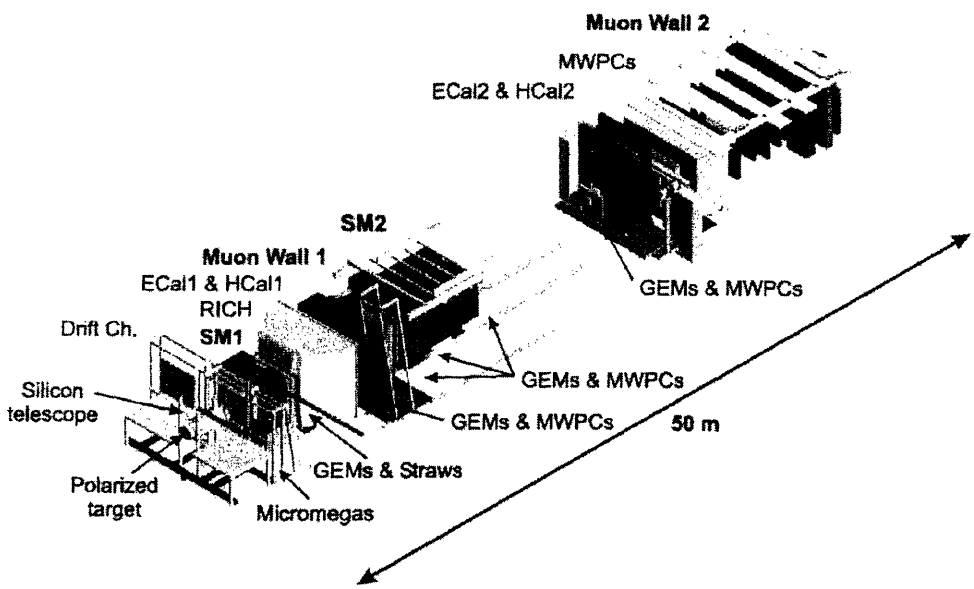

Figure 1-2: Schematic of COMPASS apparatus at CERN. Illustration reproduced from Ref. [4].

Early GEM detectors experienced damaging spark discharges when exposed to heavily ionizing particles. A GEM's discharge probability is higher for larger voltages and also increases with the presence of any local hole imperfections (e.g. etching defects or pieces of conductive debris). The COMPASS group solved this problem by testing the high-voltage stability of the GEM foils in dry nitrogen (only GEMs with leakage currents below 5 nA at 550 V were deemed acceptable) and by using triple

GEMs instead of single GEMs. By cascading three GEMs, ionization tracks could be amplified by a factor of $\sim$ 8000 at much lower voltages than needed to produce similar amplification with a single GEM.

1.2.2 STAR

The Solenoidal Tracker at RHIC (STAR) [6, and references therein] is being used at the Relativistic Heavy Ion Collider (RHIC) at Brookhaven National Lab (BNL) to study collisions between gold nuclei

$$\mathrm{Au} + \mathrm{Au} \rightarrow \quad \sim 200\text{–}4000 \text{ particles}. \tag{1.2}$$

The primary goal of the experiment is to find signs of the formation of the quark-gluon plasma (QGP) among the hundreds of tracks of the resulting particles (see Figure 1-3). This extremely dense state of matter, consisting of deconfined quarks and gluons, is predicted by QCD and is believed to have existed shortly after the Big Bang [7].

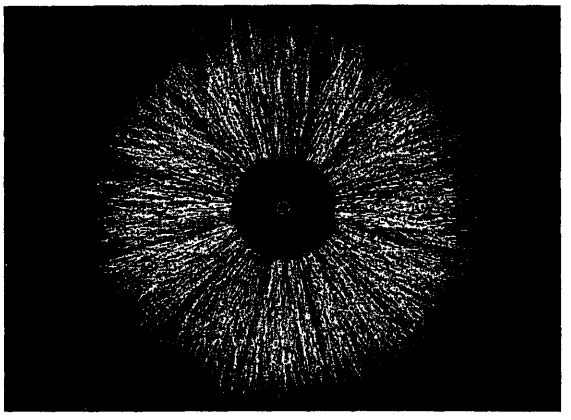

Figure 1-3: Reconstruction of particle tracks in STAR time projection chamber (TPC) from Au-Au collision. Image reproduced from Ref. [6].

The STAR apparatus is depicted schematically in Figure 1-4(a). B. Surrow and associates [8] plan to improve tracking in the forward region by installing an array of triple GEM detectors projecting ionization tracks onto fine-grain pad planes. This Forward GEM Tracker is illustrated in Figure 1-4(b). In the extremely harsh radiation

environment of STAR, spark discharges could pose a serious problem. For each of the tracker's several hundred GEMs to operate flawlessly, quality control at a level exceeding anything previously attempted will have to be implemented. The scanner described in Chapters 4 and 5 will initially be used for this purpose.

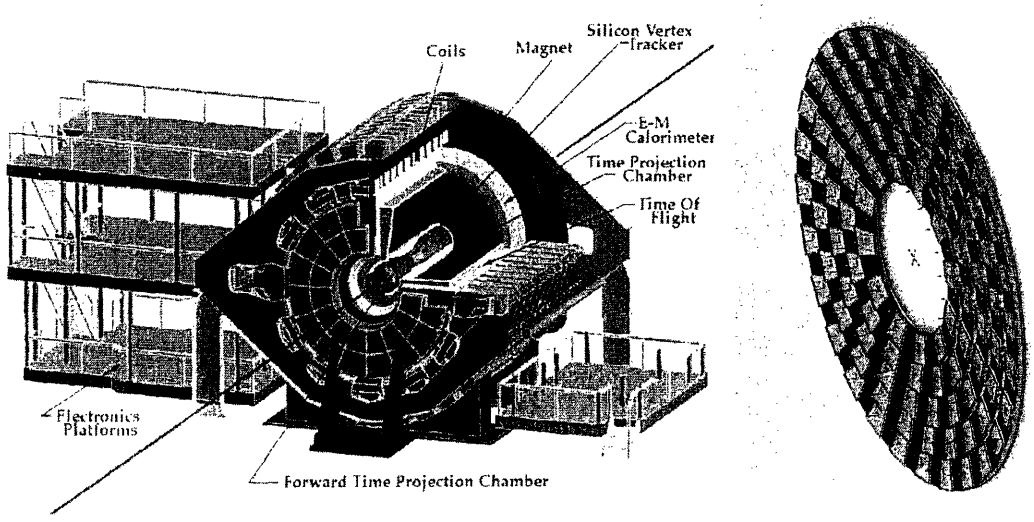

(a) (b)

Figure 1-4: Schematic of STAR apparatus (a) with detail of Forward GEM Tracker upgrade (b). Illustrations reproduced from Ref. [8].

1.2.3 ILC

The International Linear Collider (ILC) [9, 10, 11], planned to be built over the coming decade, will study the most fundamental of physical processes, the creation of mass. According to the Standard Model, the masses of the W and Z bosons, quarks, and leptons are generated through interactions with the field carried by the Higgs boson. Undeniable proof of the existence of the Higgs has yet to be obtained, though a possible Higgs signal at CERN's Large Electron and Positron (LEP) collider places the Higgs mass at $M_H \approx 115$ GeV with a 2σ upper bound of ~ 200 GeV, well within the planned TeV range of the ILC. A Standard Model Higgs H^0 is expected to be produced at the ILC primarily through the Higgs-strahlung process

$$e^+e^- \rightarrow ZH^0 . \tag{1.3}$$

The Standard Model prediction of the decay products of the Higgs depends on M_H. Decays into pairs of fermions $f\bar{f}$ dominate for $M_H \lesssim 140$ GeV, while decays into WW^* pairs dominate for $M_H \gtrsim 140$ GeV.

Measurements of the momenta of the resulting particles will be obtained by reconstructing the ionization tracks through a large (38 m^3 gas volume) cylindrical time projection chamber (TPC) in a strong (4 T) magnetic field. Achieving the desired momentum resolution of $\delta(1/p_t) < 2 \times 10^{-4}$ $(\mathrm{GeV/c})^{-1}$ will require sub-millimeter track reconstruction accuracy. GEMs are considered the optimal readout technology for this task. The high hole density permits good track projection resolution, and the ability to cascade several GEMs allows significant suppression of ion feedback. In traditional wire-chamber TPCs, positive ions created in an avalanche near a sense wire and slowly migrating toward the cathode disturb the otherwise uniform electric field in the large volume. R&D with triple GEMs in conditions similar to those planned for the ILC TPC has produced measurements of the fractional ion feedback (defined as the ratio of positive charge collected at the drift electrode to electron charge collected at the readout anode) as low as 2.5% [12]. New foil geometries may reduce ion feedback even further. The scanner of Chapters 4 and 5 will aid in the development of such GEMs at MIT.

1.2.4 X-Ray Imaging

Several groups are pursuing GEM-based medical imaging devices [13, 14]. Low intensity x-rays can be stopped in high-Z gases such as Xe and Kr. Since GEMs can be used to generate a measurable signal from the relatively small number of ionization electrons produced by a single photon, diagnostic images could be created with x-ray doses several orders of magnitude smaller than with traditional film-based imagers.

H. Bradt and R. Remillard [15] have proposed using 31 double GEM detectors to build a space-based all-sky x-ray monitor for observing short-duration explosive phenomena in the universe. A schematic of one of the 31 cameras for this Advanced X-Ray Monitor (AXM) is shown in Figure 1-5. Extensive quality control would obviously be needed to ensure reliable operation of these GEMs in an orbiting system.

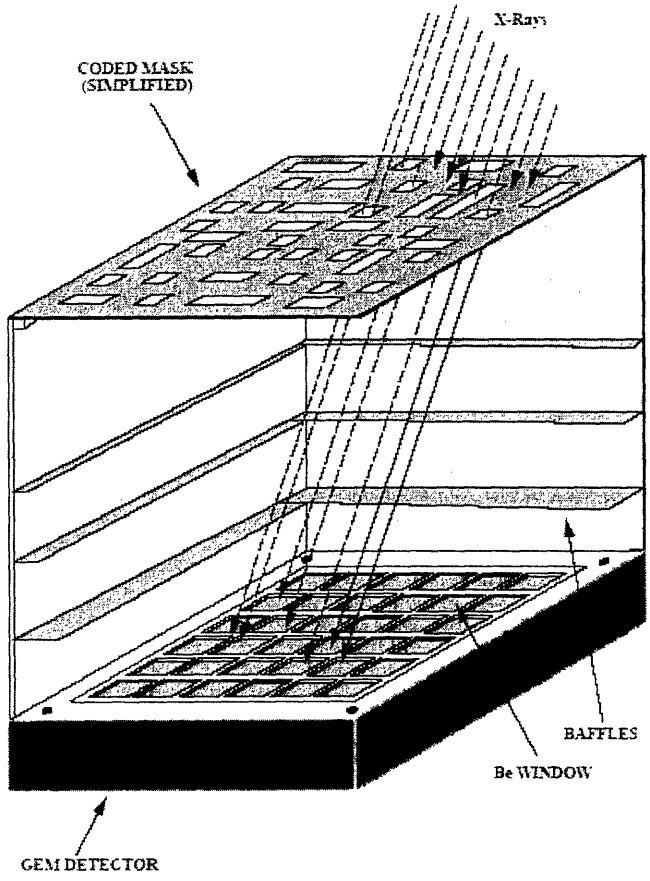

(a)

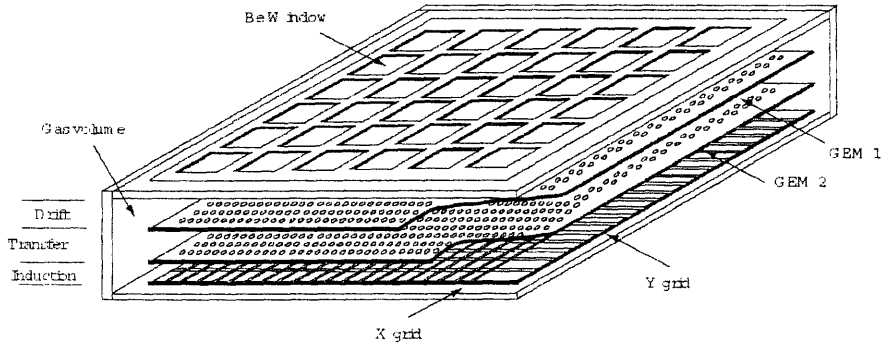

(b)

Figure 1-5: Schematic of AXM camera assembly (a) with detail of double GEM detector (b). Illustrations reproduced from Ref. [15].

1.3 Performance Variation Among GEMs of Different Manufacturers

Though CERN developed the first GEMs and has successfully produced and installed GEMs in detectors for the COMPASS experiment, CERN remains a research institution, and Sauli and others do not manufacture GEMs on a large scale. Development of a domestic source of GEMs has been initiated by U. Becker with Tech-Etch.[1] A trial run has also been completed at 3M [16].

B. Azmoun et al. [17] have performed a systematic comparison of triple GEM detectors built with GEMs from the each of the three current suppliers. For a given foil potential, they found that the effective detector gain (defined as the ratio of total collected charge to primary ionization charge) for 3M GEMs was larger than that for CERN GEMs by roughly an order of magnitude, and the gain for Tech-Etch GEMs lay between the gains for the other two foil types. While foil thickness and hole spacing were the same for all three types, the hole diameters varied. As Chapters 2 and 3 will explore in detail, GEM performance depends critically on the geometry of the foil. The observed variations in the performance of GEMs from different manufacturers is likely due, in large part, to differences in the diameters and cross-sectional shapes of the GEM holes.

1.4 Need for Automated Quality Control

Meeting the growing demand for large numbers of GEMs capable of performing reliably in high luminosity conditions requires stringent quality control.

As was suggested in the previous section, the effective gain of a GEM is strongly dependent on the foil's hole geometry. Figure 1-6, which shows measurements by J. Benlloch et al. [18] of detectors built with CERN GEMs of several different hole diameters, illustrates the dependence of effective gain on diameter. Ensuring the consistency of gain among foils as well as gain homogeneity over the area of a single

[1] Tech-Etch, Inc., Plymouth, MA, `www.tech-etch.com`.

foil requires careful regulation of the manufactured hole diameters.

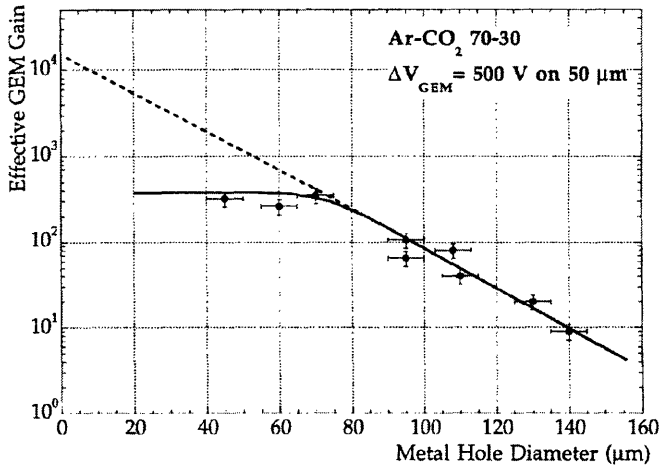

Figure 1-6: Measured effective gains of CERN GEMs as function of hole diameter. Plot reproduced from Ref. [18].

A 100 cm^2 GEM with a 140 μm pitch hexagonal hole pattern contains roughly 600,000 holes, and an irregularity in just one of these holes can render the entire GEM useless. A piece of copper debris within a GEM hole can induce a spark discharge between the foil's copper layers. The energy of such a discharge is

$$W_{\text{dis}} = \frac{1}{2} C_{\text{GEM}} (\Delta V_{\text{GEM}})^2 , \tag{1.4}$$

where C_{GEM} is the foil capacitance (4.8 nF for a 100 cm^2 Tech-Etch GEM), and ΔV_{GEM} is the potential applied between the GEM's copper surfaces. For a typical foil potential $\Delta V_{\text{GEM}} = 500$ V, the discharge energy is $W_{\text{dis}} = 6.0 \times 10^{-4}$ J. Such energy has been found sufficient to burn away copper and Kapton between GEM holes at the sparking sites.

To ensure gain homogeneity and to limit the probability of damaging discharges, one would like to measure the diameter of each hole and locate every etching defect and piece of debris which could lead to premature foil failure. Manual spot-checking of GEMs under an optical microscope can be used to measure hole diameters and provide a rough idea of the density of etching defects but is extremely labor-intensive, and an operator is unlikely to locate every flaw among the 600,000 holes.

An automated scanner capable of optically inspecting every hole would provide the requisite level of quality control with minimal operator input. Such a device has been constructed. Details of its development are the topic of Chapter 4, and the results of scans performed on recently-manufactured Tech-Etch GEMs are described in Chapter 5.

Chapter 2

Function and Geometry

This chapter begins with a brief discussion of the function of a GEM in a gaseous particle detector such as a TPC. A detailed description of GEM geometry follows. This material provides the background needed for the discussion of the physics of GEM operation in Chapter 3.

2.1 Basic Function

A gas-filled drift chamber such as a TPC can be used to reconstruct the trajectories and measure the energies of particles produced in a high-energy experiment. A possible TPC configuration using a single GEM is illustrated schematically in Figure 2-1. Such chambers are typically filled with a gas mixture, containing primarily Ar with CH_4 or CO_2 added as a quencher, near atmospheric pressure.

A charged particle or photon entering the detector window ionizes gas atoms along its trajectory. The liberated electrons move in a drift field of magnitude E_D toward the upper surface of the GEM. A voltage ΔV_{GEM} (on the order of 500 V) applied between the upper and lower surfaces of the GEM creates a strong electric field (on the order of $\Delta V_{\mathrm{GEM}}/T = 500$ V/50 μm $= 10^5$ V/cm) within the GEM holes. In this field, the primary electrons acquire enough energy between random collisions with gas atoms to cause secondary ionization. An electron avalanche results, and secondary electrons exiting the GEM holes move through an induction field of magnitude E_I

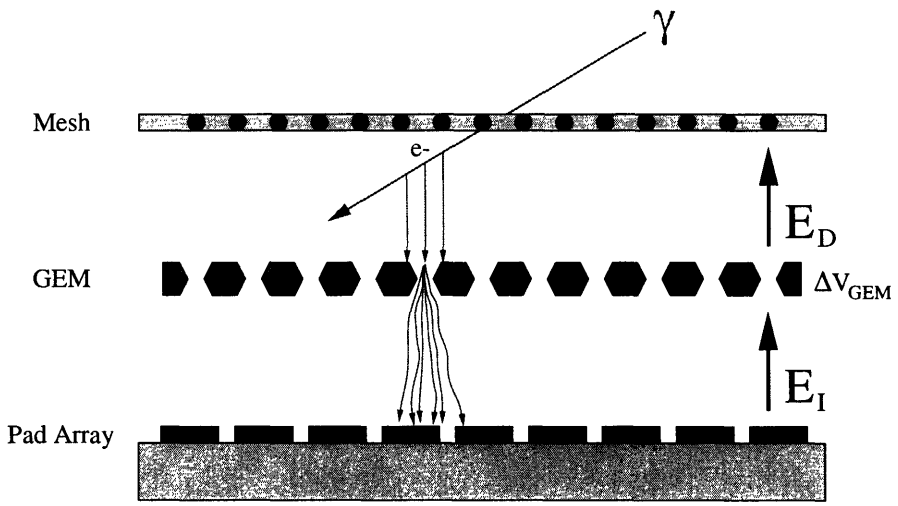

Figure 2-1: Schematic illustration of GEM as element of TPC.

toward a two-dimensional array of pads. Charge collected on each of these pads produces a pulse of current. In a TPC the coordinates of the pads producing finite signals can be combined with the times at which the signals were observed as well as pre-existing electron drift velocity measurements to reconstruct the particle's path in three dimensions. If E_{inc} is the initial energy of the incident particle and W the energy required for that particle to produce a single electron-ion pair, then the total charge produced along the particle's track is $N_0 = E_{\text{inc}}/W$. The sum of the integrals of the pad signals should be proportional to E_{inc}.

The role of the GEM is to amplify the small number N_0 of electrons in the charge cluster produced by an initial ionization event into a measurable signal. The most important characteristic of a GEM, therefore, is its "effective gain"

$$G_{\text{eff}} \equiv \frac{\text{number of electrons in signal}}{N_0}. \tag{2.1}$$

This parameter links the actual ionization events to the magnitudes of the measured signals. It depends upon but is not the same as the multiplicative hole gain

$$G \equiv \frac{\text{number of secondary electrons exiting hole}}{\text{number of primary electrons entering hole}}. \tag{2.2}$$

As will be discussed in Section 3.2.3, this distinction exists because not all primaries

enter holes, and not all secondaries reach the pad plane. Effective gains on the order of 10^2–10^3 have been observed experimentally with typical foil geometries [19]. Even greater gains (approaching 10^5) can be obtained by cascading two or three foils to form double or triple GEMs [17].

2.2 Geometry

GEM geometry is defined by the pattern in which the holes are distributed, the hole cross-sectional shape, and the hole diameter. The geometric parameters are shown schematically for the most widely used hexagonal double-conical design in Figure 2-2. A cross-sectional view is drawn above a planar view looking in a direction normal to the GEM surface. For Tech-Etch GEMs, these parameters typically have the following values: $P = 140$ μm, $D = 80$ μm, $d = 50$ μm, $T = 50$ μm, and $t = 5$ μm.

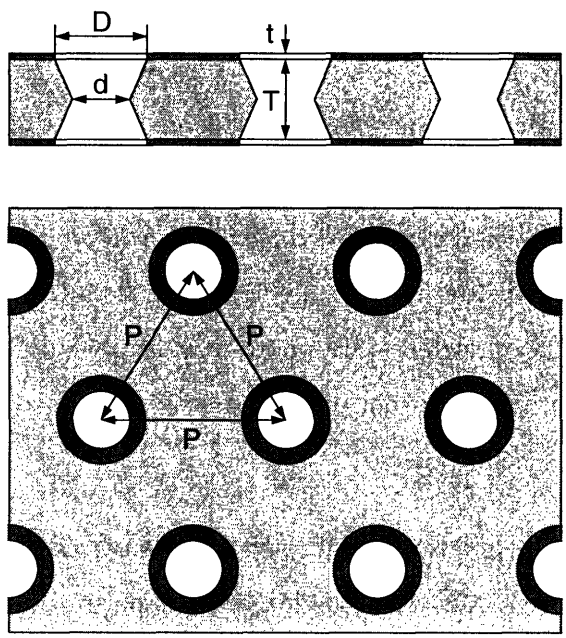

Figure 2-2: Illustration of hexagonal double-conical GEM geometry.

2.2.1 Hole Pattern

Holes can be distributed in either a square or hexagonal pattern with a pitch, or separation between holes, of size P. The earliest GEMs, like that shown in Figure 1-1, used a square hole pattern, while more recent foils have used a hexagonal pattern as shown in Figure 2-2. The choice of pattern and pitch affects the GEM's optical transparency τ, the ratio of hole area to total copper area. Expressions for this quantity

$$\begin{aligned} \tau_{\text{sq}} &= \frac{\pi}{4}\left(\frac{D}{P}\right)^2 \\ \tau_{\text{hex}} &= \frac{\pi}{2\sqrt{3}}\left(\frac{D}{P}\right)^2 , \end{aligned} \tag{2.3}$$

where D is the copper hole diameter, indicate that τ_{hex} is larger than τ_{sq} by about 15%. The advantage of a larger optical transparency will be made clear in Section 3.2.3.

2.2.2 Hole Shape

The cross-sectional shape of a GEM hole can be one of three primary types:

- **Double-Conical:** An hour-glass-shaped hole with diameters D at the two copper surfaces larger than the diameter d in the middle of the Kapton. Diameters D and d will be referred to as *copper* and *Kapton* diameters respectively for the remainder of this thesis. This shape results from the manufacturing process in which the copper surfaces are photo-lithographically etched with acid, and the dielectric core exposed between the newly-formed copper holes is dissolved with a Kapton-specific solvent.

- **Cylindrical:** A hole with straight sides and a constant diameter through the entire foil thickness. GEMs with this hole shape were found to be superior to double-conical GEMs in terms of gain stability under irradiation (lacking an initial rise seen in the latter type due to charging of the dielectric) but often suffered from over and under-etching of the Kapton [19].

- **Single-Conical:** A cone-shaped hole with a wide diameter on one copper surface and a narrow diameter on the other. The GEM can either be oriented with the wide side or the narrow side toward the source of irradiation. Both variations have been produced and studied at CERN [19].

The results of simulations by O. Bouianov [20] indicate that the charge transfer processes, and hence the effective GEM gains, are very different for foils with different hole shapes. Because the double-conical shape is currently the most widely used, however, the rest of this chapter and all of Chapter 3 will assume this shape.

2.2.3 Hole Diameter

Both the copper and Kapton diameters of a double-conical GEM can be selected to optimize detector performance.

The choice of copper diameter influences the effective gain G_{eff} through two mechanisms. Firstly as indicated in Eq. 2.3, optical transparency τ is an increasing function of D. Secondly, the electric field in the hole is a decreasing function of D. As will be shown in Section 3.2, G_{eff} is strongly dependent upon both optical transparency and the magnitude of the field within the hole.

As was suggested in the discussion of cylindrical geometry, the Kapton diameter should be made as close to the copper diameter as possible. Kapton in a double-conical hole experiences a "charging-up" effect under irradiation [21]. Initial gain instability of double-conical GEMs (not observed in conical GEMs) has been attributed to this effect [19]. The optimal Kapton diameter, therefore, would seem to be one as close to the copper diameter as can be reliably manufactured.

Chapter 3

Physics of GEM Operation

This chapter describes the physical principles inherent in GEM operation. It includes a discussion of electrostatics followed by a description of the physical mechanism of charge amplification.

3.1 Electrostatics

The electric field through a hole of a GEM with voltage ΔV_{GEM} applied between its copper surfaces can be understood on the basis of simple electrostatic considerations. A GEM is essentially a perforated parallel plate capacitor with separation T. By the superposition principle, the field of such a capacitor is just the sum of the field of an unperforated capacitor and the fields of pairs of parallel hole-sized conductive disks centered at each hole location. This idea is illustrated schematically in Figure 3-1. Note that the field of a pair of oppositely charged disks should be approximately dipole at distance $r \gg D$, and, therefore, the field in each GEM hole must have a dipole form.

The magnitude of the field at the center of a hole can be readily estimated. It must be lower than the parallel plate value of $\Delta V_{\mathrm{GEM}}/T$, since the field between the disks is directed opposite the parallel-plate field as illustrated in Figure 3-1. One should expect this magnitude to be a decreasing function of hole diameter, approaching $\Delta V_{\mathrm{GEM}}/T$ in the zero-diameter limit. Assuming a constant charge density

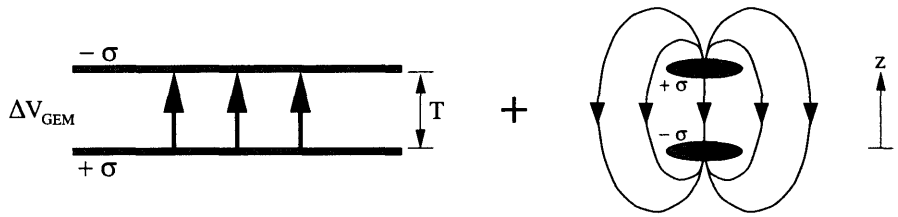

Figure 3-1: Illustration of electrostatic field in GEM hole as superposition of parallel-plate and parallel-disk fields.

$\sigma = \epsilon_0 \Delta V_{\mathrm{GEM}}/T$ (ignoring the dielectric), the field of the two disks along the line joining the disks' centers can be calculated analytically and added to the parallel-plate field to give an expression for the electric field at the center of the hole

$$\vec{E} = \frac{E_0}{2}\left[\frac{z}{\sqrt{z^2 + (D/2)^2}} + \frac{(T-z)}{\sqrt{(T-z)^2 + (D/2)^2}}\right]\vec{e}_z\,, \tag{3.1}$$

where $E_0 = \Delta V_{\mathrm{GEM}}/T$ is the magnitude of the parallel-plate field. The diameter dependence of E/E_0 at a point halfway between the upper and lower GEM surfaces ($z = T/2$) is plotted for $T = 50$ μm in Figure 3-2(a). The z dependence of E/E_0 is plotted for several diameters and the same value of T in Figure 3-2(b). Note that the dashed vertical lines mark the positions of the upper and lower GEM surfaces.

The results of numerous calculations of the hole field using the finite-element analysis program Maxwell 3D[1] have been published [20, 21, 22, 23, 24, 25]. These calculations have incorporated the effects of the hour-glass-shaped Kapton core ignored in the previous estimates. The electric field through a double-conical GEM hole as computed by Bachmann et al. [23] is plotted in Figure 3-3. This calculation assumed the following GEM dimensions: $P = 140$ μm, $D = 70$ μm, $d = 55$ μm, $T = 50$ μm, and $t = 5$ μm. As indicated in the figure, a foil voltage of 500 V was used, and the effects of a 2 kV/cm drift field and a 6 kV/cm induction field were also included. The plot confirms the intuitive estimate of a dipole field. The Bachmann group [23] also recorded maximum values of the of the field at the centers of holes of various diameters that were within about 5% of the estimates of Figure 3-2(b).

[1] Ansoft, Pittsburgh, PA, www.ansoft.com.

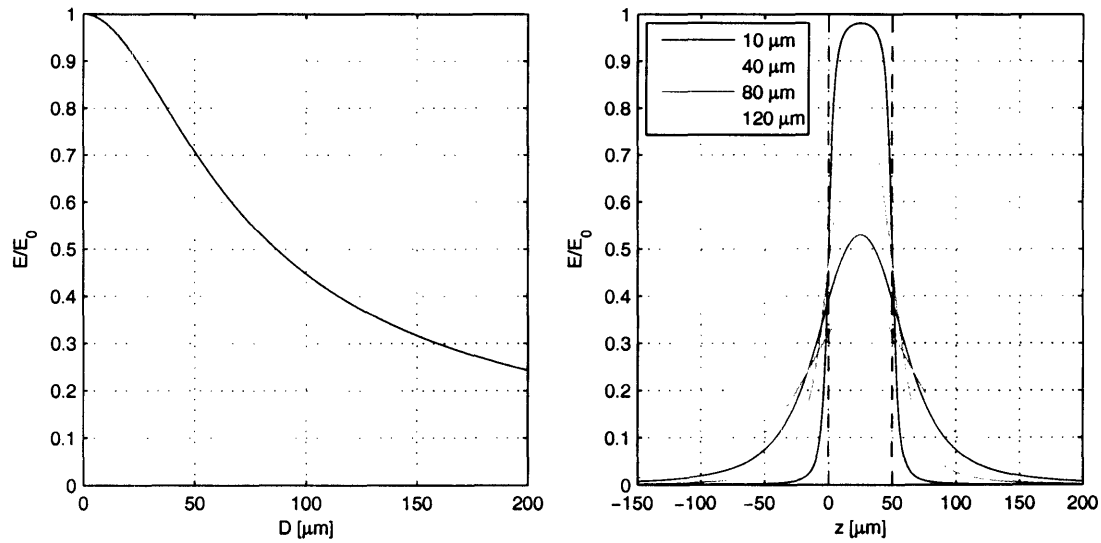

Figure 3-2: Estimated electric field magnitude (normalized by E_0) at hole center (a) as function of diameter and (b) as function of position.

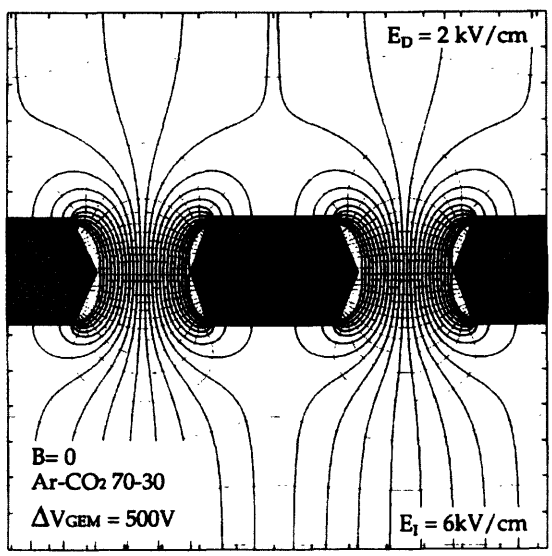

Figure 3-3: Simulated electric field through GEM hole for typical experimental conditions. Plot reproduced from Ref. [23].

3.2 Physical Mechanism of Amplification

The large field within a GEM hole allows electrons which have drifted to the upper surface of the GEM to acquire enough energy between collisions with gas atoms to cause secondary ionization. One secondary electron ionizes another gas atom, and a cascade of secondary ionization ensues through the hole.

This section begins with an estimate of the multiplicative hole gain G followed by a description of the dependence of G on the field within the GEM holes. Section 3.2.3 relates G to the the effective gain G_{eff} based on insights provided by computer simulations.

3.2.1 Estimate

One can form a rough, idealized estimate of G based on the value of an electron's mean free path λ, the characteristic distance traveled by an electron between elastic collisions with gas atoms [26]. The mean free path is a function of both the electron energy and the choice of gas and has an approximate value of 5 μm for typical noble gases at 1 atm. There exists a certain critical value of the hole field E_c at which an electron traversing a distance λ through the hole can acquire just enough energy W to ionize a gas atom. This value is simply

$$E_c = \frac{W}{e\lambda}, \tag{3.2}$$

where W, the average energy required to produce an electron-ion pair, is a function of drift gas and has an experimentally-determined value of 26.3 eV for electrons in pure argon [27, Table 1.3]. For argon then, one would expect E_c = 26.3 V/5 μm = 53 kV/cm. If the average hole field exceeds E_c, one can make the assumption that each new "generation" of secondary ionization requires the parent electrons to travel a distance of λ through the hole. The gain can thus be approximated as

$$2^{T/\lambda} = 2^{50/5} = 1024 \tag{3.3}$$

for a GEM of thickness $T = 50$ μm.

3.2.2 Dependence on Field Within Holes

The actual amount of ionization produced over a given distance depends on the electric field and is characterized by the first Townsend coefficient α [27]. The Townsend coefficient is defined such that

$$dN = N\alpha ds\,, \tag{3.4}$$

where N is the total ionization charge, and dN is the increase in ionization charge produced over distance ds. The value of α varies among gas mixtures and can only be found through experiment or simulation. α is proportional to gas density and increases with electric field. Its functional dependence can be expressed as

$$\frac{\alpha}{P} = f\left(\frac{E}{P}\right)\,, \tag{3.5}$$

where P is pressure and E electric field. The multiplicative hole gain can be computed by integrating Eq. 3.4 along a path from point s_u on the upper side of the GEM to point s_l on the lower side

$$G = \frac{N}{N_0} = \exp \int_{s_u}^{s_l} \alpha(E(s))ds\,, \tag{3.6}$$

where N is the number of secondary electrons exiting the hole, and N_0 is the number of primary electrons entering. Since $\alpha(E)$ is an increasing function of E, G must increase exponentially with E.

The exponential dependence of G_{eff} on ΔV_{GEM} is illustrated in Figure 3-4. These measurements of G_{eff} for a triple Tech-Etch GEM were obtained by U. Becker [28] for P10 (Ar-CH_4 90-10) at 1 atm. The primary charge cluster sizes were taken to be

$$N_0 = 0.9\left(\frac{E_\gamma}{W_{\text{Ar}}}\right) + 0.1\left(\frac{E_\gamma}{W_{\text{CH}_4}}\right)\,, \tag{3.7}$$

where $W_{\text{Ar}} = 26.3$ eV and $W_{\text{CH}_4} = 27.1$ eV are the average energies required to pro-

duce single electron-ion pairs in Ar and CH_4 [27, Table 1.3], and E_γ is the energy of the incident photon. For the 5.9 keV and 14.4 keV photons used in these measurements, Eq. 3.7 yields values of 224 ± 15 and 546 ± 24 respectively (with uncertainties of $\pm\sqrt{(N_0)}$ based on Poisson statistics). A high voltage source supplied power to the electrodes through a resistor network. Equal potentials ΔV_{GEM} were applied across each of the three GEMs, while the following values were used for the the drift, transfer,[2] and induction fields (in V/cm): $E_D = 3.0\Delta V_{\mathrm{GEM}}$, $E_T = 5.6\Delta V_{\mathrm{GEM}}$, and $E_I = 11.1\Delta V_{\mathrm{GEM}}$.

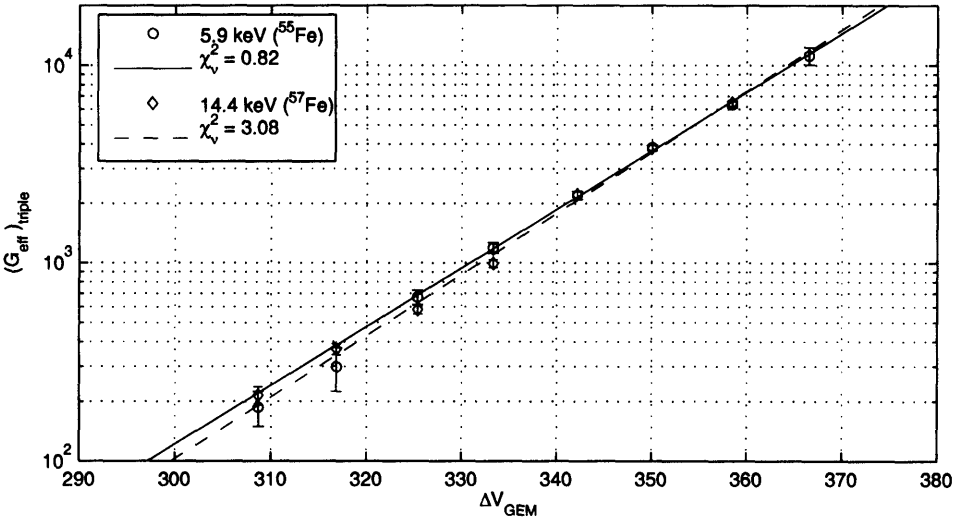

Figure 3-4: Measured effective gain of Tech-Etch triple GEM as function of foil potential (equal for each of three GEMs).

As can be seen in Figure 3-4, the gain curves for 5.9 keV and 14.4 keV nearly overlap. The signals are clearly proportional to the incident photon energy over this range.

3.2.3 Simulation Results

O. Bouianov has performed an extensive computer simulation study of GEM amplification processes [20, 21, 29]. The previous discussion has ignored the diffusion of

[2]In double and triple GEM structures, the electric field between the lower surface of one GEM and the upper surface of another is typically called a transfer field with magnitude E_T.

electrons between ionizing collisions. Bouianov has modeled diffusion effects in his simulations. As can be seen in the plot of simulated electron trajectories through a triple GEM shown in Figure 3-5, the effect of diffusion on the lateral extent of the avalanche can be significant. Largely because of diffusion, not all primary electrons enter the amplification holes, and not all secondaries enter the induction region.

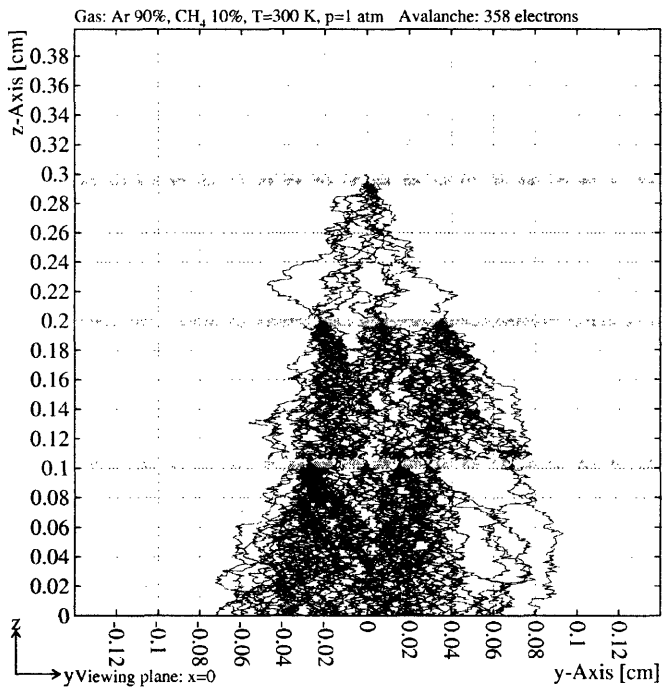

Figure 3-5: Simulated electron trajectories through triple GEM. Plot reproduced from Ref. [29].

Following Bouianov's approach [21], one can express the effective GEM gain G_{eff} as the product of four factors

$$G_{\text{eff}} = E_{\text{pr}} G E_{\text{sc}} C \,, \tag{3.8}$$

where each term is defined as follows:

- **Primary electron transparency E_{pr}:** Fraction of primary electrons that actually enter the GEM holes. E_{pr} is an increasing function of both optical transparency τ and GEM voltage ΔV_{GEM}. While Figure 3-3 shows all field lines

in the drift region entering the hole, diffusion causes a fraction of the primaries to be lost to the upper surface of the GEM.

- **Multiplicative hole gain G:** Ratio defined in Eq. 2.2.
- **Secondary electron collection efficiency E_{sc}:** Fraction of secondary electrons produced in GEM holes that travel through induction field. Some secondaries are lost to either the dielectric or the lower copper surface.
- **Induced charge factor C:** Besides the secondary electron charge itself, the total current produced on a readout anode includes an additional approximately equal induced component due to the movement of the secondaries through the induction field. Thus, $C \approx 2$.

Eq. 3.8 also yields a simple relation between the effective gain of a single GEM G_{eff} and the effective gain of a triple GEM $(G_{\mathrm{eff}})_{\mathrm{triple}}$

$$(G_{\mathrm{eff}})_{\mathrm{triple}} = 2\left(\frac{G_{\mathrm{eff}}}{2}\right)^3, \tag{3.9}$$

using the assumption $C = 2$.

Chapter 4

Scanner for Quality Control

This chapter details the development of an automated GEM scanner. The scanner is essentially a dedicated microscope with automated video image capture and stage positioning capability combined with feature measurement and flaw detection software (GEMScan) programmed in MATLAB.[1] The system's hardware and software were designed specifically for the automated quality control of GEMs.

A single scan takes less than 30 minutes to examine more than 600,000 holes. The machine can measure either the inner Kapton or outer copper diameters of every hole in a GEM. It simultaneously locates and geometrically classifies potential foil defects by identifying areas of the GEM with hole pattern irregularities.[2] At the conclusion of a scan, the software automatically generates a GEM quality report containing hole diameter and pitch histograms and plots of diameter homogeneity and the spatial distribution of defects. A graphical interface permits a user to review images of problem areas.

The chapter begins with a description of the scanner motion control and imaging hardware, followed by a summary of the key features of the data acquisition and processing software and a description of techniques for calibrating the apparatus.

[1]The MathWorks, Inc., Natick, MA, www.mathworks.com.

[2]The scanner has been programmed to handle both hexagonal and square hole patterns. A scan of the outer copper diameters of a segmented GEM would require a modification of the current software.

4.1 Hardware

The primary hardware components can be seen in the photograph and the schematic in Figures 4-1 and 4-2 respectively. As illustrated in the schematic, a GEM is secured between two 1/4" sheets of glass which are pressed together by a pair of aluminum frames. This glass platform sits atop a pair of servo-driven linear stages. A long zoom macro lens with attached video camera is suspended above the stages and platform by an aluminum support bridge. A set of rails and a 1/4-28 lead screw mounted to the bridge permit coarse focus adjustments of the lens. A white LED ring light is secured at the base of the lens to provide front illumination of the GEM. A white LED backlight for rear illumination is held by a cantilever support bracket beneath the glass platform. During a scan, the platform-mounted GEM moves, while the imaging components (camera, lens, and lights) remain stationary. The entire apparatus is bolted to a 1/2" aluminum plate and placed on a solid steel 1-ton lift table to limit mechanical vibration.

4.1.1 Motion Control

The selection of stages to position a GEM beneath the camera was guided by the following constraints:

- **Encoder Resolution:** A scan consists of numerous overlapping images. To accurately measure the distance between features in adjacent image frames, the encoder resolution had to be small relative to the hole pitch. For a typical pitch of 140 μm, a resolution well under 10 μm would be needed.

- **Positioning Repeatability:** An open-loop design using stepper motors or even a closed-loop design using servos with rotary encoders would accumulate significant error over the scan path due to lead screw backlash and other mechanical imperfections. Linear encoders, however, would provide a measure of the actual stage positions regardless of backlash or motor over/undershoot.

- **Operating Envelope:** A Tech-Etch GEM is 10 $\times$ 10 cm. The travel of each

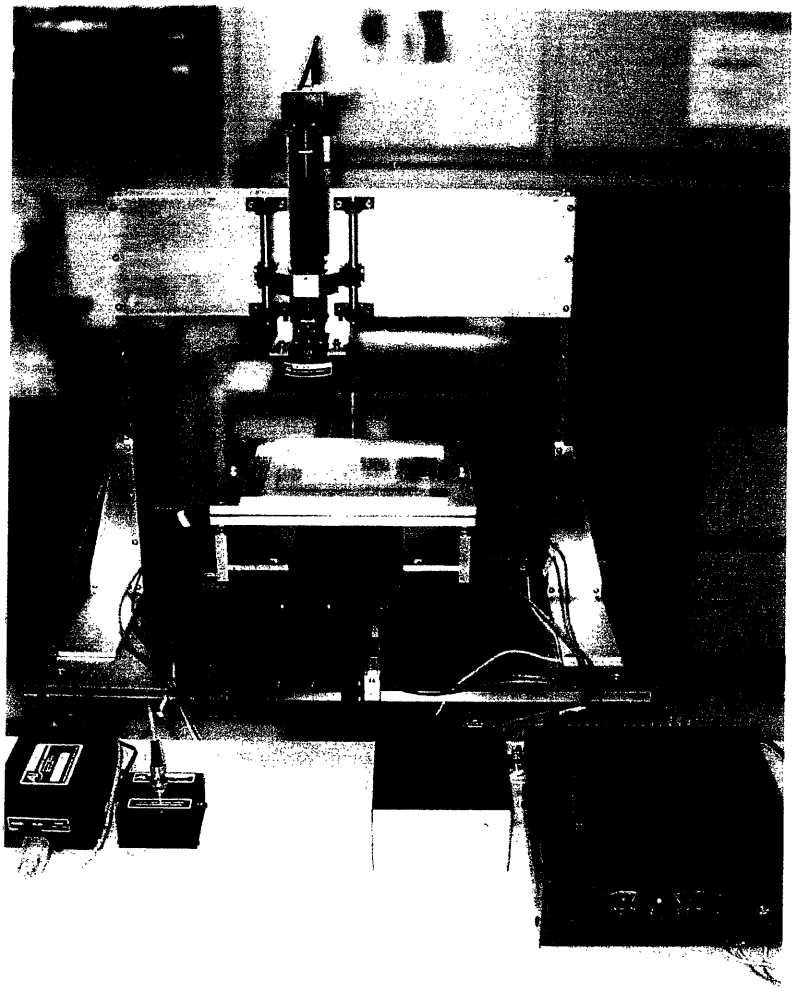

Figure 4-1: Photograph of scanner apparatus.

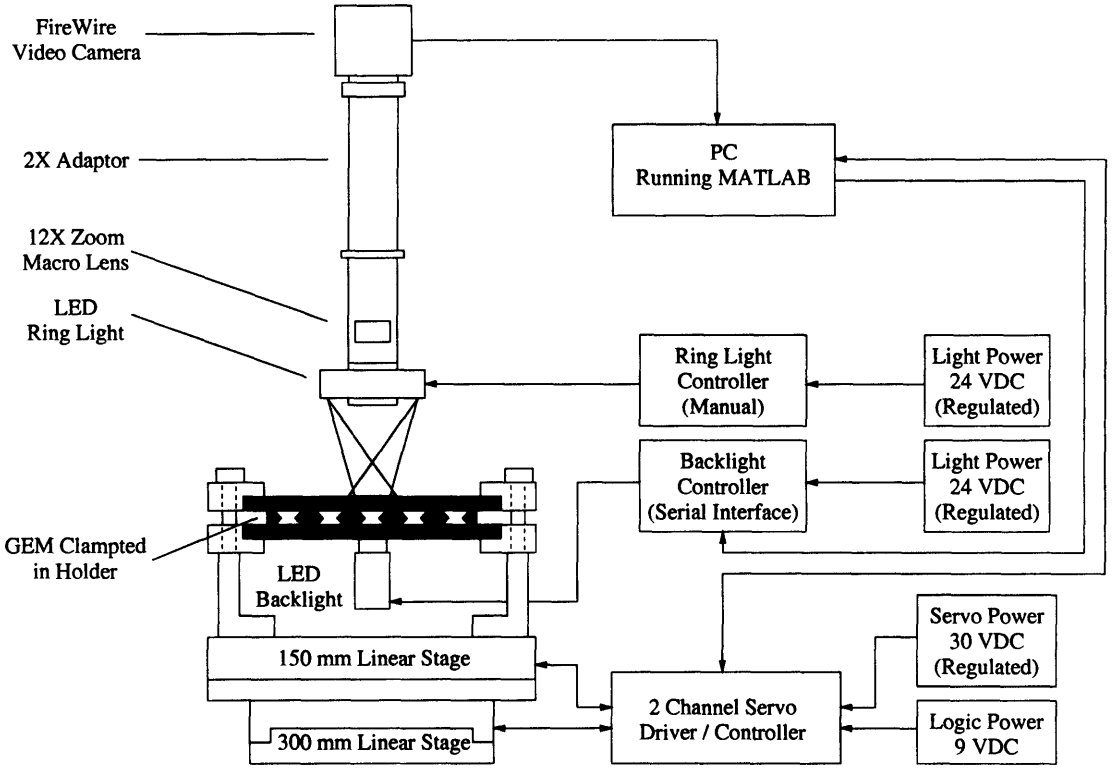

Figure 4-2: Schematic of scanner apparatus.

stage had to exceed 10 cm.

Two linear servo-driven stages with glass-scale linear encoders were ultimately chosen. Both stages were manufactured by Newport[3] and feature encoders produced by Heidenhain.[4] The 150 mm TS150DC, with a 0.5 μm resolution LIF12R encoder mounted along the center of the underside of the moving platform, is used for the x-axis. The 300 mm TS300DC, with a 1.0 μm resolution LS473 encoder mounted along the side of the moving platform, is used for the y-axis.

The stages are controlled by combination servo driver/controller cards manufactured by J.R. Kerr.[5] Two PIC-Servo Motion Control Boards, daisy-chained together and connected to a Z232-485 Serial Port Converter Board, are housed in a custom case. A regulated variable power supply set to roughly 30 VDC provides power to the stage servos, and an unregulated 9 VDC wall adaptor supplies logic power. The

[3]Newport Corporation, Irvine, CA, `www.newport.com`.
[4]Heidenhain Corporation, Schaumburg, IL, `www.heidenhain.com`.
[5]Jeffrey Kerr, LLC, Flagstaff, AZ, `www.jrkerr.com`.

controller is linked to the stages with a pair of custom multi-conductor cables and communicates with the PC through a serial connection.

The driver/controller receives positioning commands from the PC and drives each stage servo with a pulse-width-modulated (PWM) voltage regulated by a position-integral-derivative (PID) control loop. A dynamic link library (DLL) provided by the manufacturer is loaded into MATLAB to access the functions needed to specify goal positions; read out encoder positions; and tune the servo velocities, accelerations, and control loop gains.

Positioning error can be characterized by both the absolute accuracy of the encoders and the positioning repeatability of the stages. Calibration data from the manufacturer indicates an absolute uncertainty of ± 1.5 μm over the full 150 mm range of stage-x and an absolute uncertainty of ± 2 μm over the full 300 mm range of stage-y. A measure of the positioning repeatability of the stages was obtained by using the GEMScan individual feature measurement tool to see how the apparent position of a single hole in the upper-left corner of a GEM varied with accumulated stage travel. The centroid of the hole was measured and then remeasured following a 20 cm round trip of stage-x or stage-y. This process was repeated 15 times for each stage. The results plotted in Figure 4-3 indicate that both stages maintained their positions within 1 to 2 encoder increments over 300 cm of accumulated travel.

4.1.2 Imaging

The scanner imaging system consists of a video camera, a zoom macro lens, a ring light, and a backlight.

Images are captured using a FireWire video camera. The DFK 21F04 from The Imaging Source[6] is based on the Sony ICX098BQ, a 1/4" color CCD with a resolution of 640×480 pixels. A FireWire connects the camera to the computer's FireWire port. The camera attaches to the lens via standard C-mount threads.

Magnification is provided by the 12X Zoom from Navitar.[7] The scanner uses a

[6]The Imaging Source, Charlotte, NC, `www.theimagingsource.com`.
[7]Navitar, Inc., Rochester, NY, `www.navitar.com`.

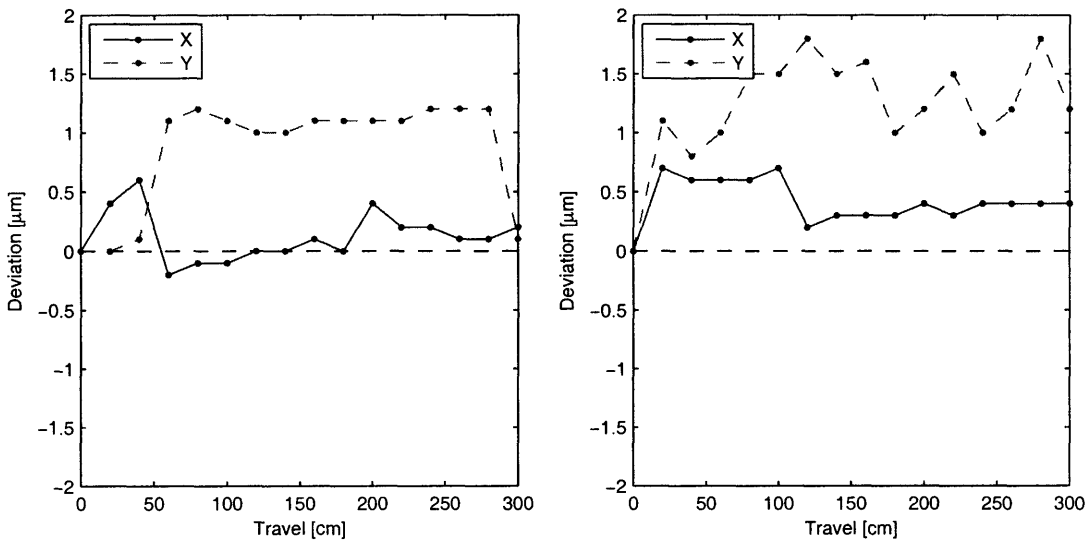

Figure 4-3: Deviation in measured position of GEM corner hole versus accumulated travel of stage-x (a) and stage-y (b).

variant (1-50486) of the standard model that includes 12 mm of fine focus at the base of the lens barrel. A C-Mount Coupler (1-6010) and a 2X Adaptor (1-6030) connect the lens to the camera. High-contrast images can be produced for magnifications in the range of 1–4 μm/pixel.

An LED ring light provides even illumination of the front of a GEM during a copper hole scan. Because the copper surface is much more reflective than the Kapton core, holes under front lighting appear black against a light copper background. The RL1424-WHI100M, from Advanced Illumination,[8] features white LEDs. The light is powered by the Advanced Illumination CS100-IC Variable Current Supply.

An LED backlight shines through the underside of a GEM during a Kapton hole scan. The backlit holes appear white against the black background of the unlit front copper surface. The BL5420-WHI20, also from Advanced Illumination, produces a 20 mm spot of white LED light. Because Kapton diameter measurements are very sensitive to variations in backlight intensity, an intensity controller with a computer control interface was selected to improve measurement repeatability. The Advanced Illumination S4000 Signatech Controller allows the backlight current to be adjusted

[8]Advanced Illumination, Rochester, VT, `www.advancedillumination.com`.

using a software interface which communicates with the controller through the computer's serial port.

4.2 Software

To permit rapid prototyping and implementation of data processing algorithms, the software was written entirely in MATLAB.[9] The final version of the software, called GEMScan, regulates all aspects of the scanning procedure including scanner setup and calibration, data acquisition, data processing, foil violation review, and automatic quality report generation.

This section begins with an overview of the sequence of events that takes place each time GEMScan performs a scan. The software interface is then briefly described. Summaries of the data acquisition and data processing techniques follow.

4.2.1 Operation Sequence

An overview of the sequence of events needed to scan and process a GEM is useful before discussing the algorithms of a particular operation in any detail. A complete characterization of a GEM requires the repetition of each of the following steps (with the exception of setup and calibration) four times, one scan of copper holes (using the ring light) and one scan of Kapton holes (using the backlight) on each side of the GEM:

1. **Scanner Setup and Calibration:** Before a scan can begin, the apparatus must be calibrated. The relation between camera pixels and stage positions must be established, the boundaries of the current scan region must be set, and the camera and lights must be adjusted to permit accurate hole diameter measurements. These calibrations are described in Section 4.3.

2. **Data Acquisition:** Hole positions and diameters are recorded as the stages

[9]MATLAB 7.0.1 with the Image Acquisition Toolbox 1.7 and the Image Processing Toolbox 5.0.1 were used in the final software implementation.

scan the GEM under the camera. At each stage position, a still image is captured, and the data for each hole (or any other high-contrast feature) in the image is recorded. Section 4.2.3 presents the details of the data acquisition procedure.

3. **Data Processing:** The position and diameter data at this point exists only as vectors with at least as many elements as the GEM has holes.[10] GEMScan uses a number of very simple yet robust algorithms to extract from these vectors the nature and location of possible foil defects. Section 4.2.4 describes the essential details of these algorithms.

4. **Report Generation:** As soon as the data has been processed, GEMScan automatically generates a GEM quality report. This report consists of hole diameter and pitch histograms and plots of diameter homogeneity and the spatial distribution of defects.

5. **Violation Image Capture:** While the information contained in the quality report provides a fairly good measure of the quality of the GEM, a user with a little more time to spend on each GEM can opt to actually view each foil defect. GEMScan moves the stages back to each region of the GEM containing a flaw and captures a digital image.

6. **Violation Review:** At any time after image capture, a user can load the scan data and violation images for review. The images are displayed one at a time in the GEMScan user interface with all violations highlighted. A user can classify each violation according to cause (e.g. a piece of dust or an incomplete etch). A table of classified violations is automatically generated upon completion of the review.

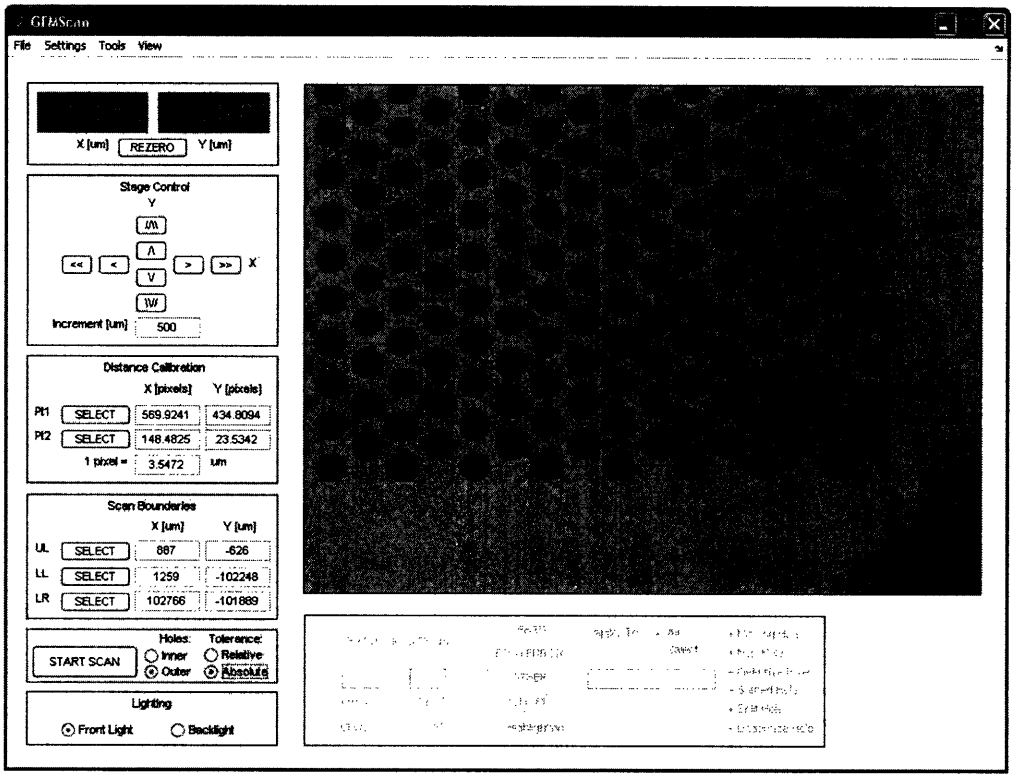

Figure 4-4: Screen shot of GEMScan user interface.

4.2.2 User Interface

A user accesses the many functions of GEMScan through the graphical user interface pictured in Figure 4-4. As can be seen in this screen shot, an image from the camera occupies the bulk of the window. The current stage position is displayed in the upper-left corner. A graphical joystick just below the position display permits manual positioning of the stages. Below the joystick are controls to calibrate the apparatus and to set the boundaries of the current scan. Below the camera image (the area appears ghosted in Figure 4-4) are controls for violation review. Various user-settable parameters as well as utility functions for measuring individual features, saving single images, and controlling the image display are accessible through the menus visible at the top of the window.

[10]Due to overlap between image frames, some holes are captured in multiple frames.

4.2.3 Data Acquisition

The data acquisition process consists of measuring the positions and diameters of all the holes of a GEM. This step consumes the majority of the total scan time, roughly 25 minutes for a typical magnification setting of 3.5 μm/pixel.

4.2.3.1 Scan Technique

A GEM is scanned by incrementally moving the stages back and forth along a zig-zag trajectory as illustrated schematically in Figure 4-5. Each rectangular box in the illustration represents a position at which the stages momentarily stop so that the camera can acquire a still grayscale image.[11] A pause of about 80 ms between stopping the stages and capturing an image has been found to be necessary to prevent any image blurring introduced by mechanical vibrations induced by the rapid deceleration of the stages. The number of frames required obviously varies with magnification setting, but a 100 cm^2 GEM at 3.5 μm/pixel requires roughly 2200 images.

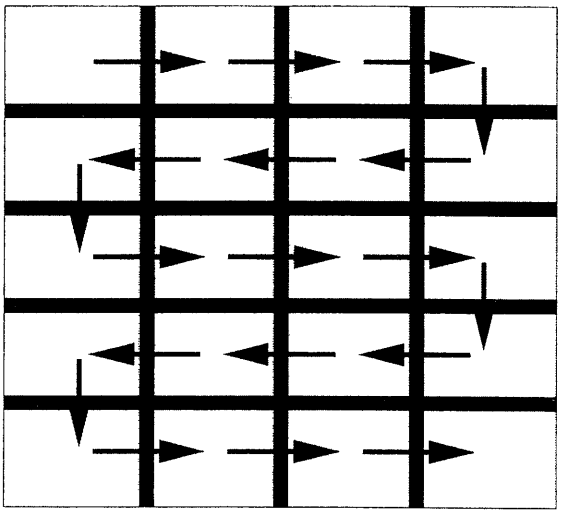

Figure 4-5: Schematic illustration of image acquisition technique.

To ensure that each hole is entirely captured within at least one frame, a finite overlap between adjacent frames is required. This overlap is represented by the darker shaded regions in Figure 4-5. Figure 4-6 shows a two-frame-wide area of a GEM

[11] Though the camera can capture color images, the camera is operated in grayscale mode to reduce image acquisition time.

overlaid with heavy lines indicating the extent of each frame. As can be seen in this illustration, a number of holes along the border of each frame are only partially visible. To avoid confusing these partially-visible holes with misshapen holes or other etching imperfections, an "ignore border" (denoted by the outermost dashed boxes in Figure 4-6) is defined such that any feature with a centroid lying outside this border is ignored within the current frame.[12]

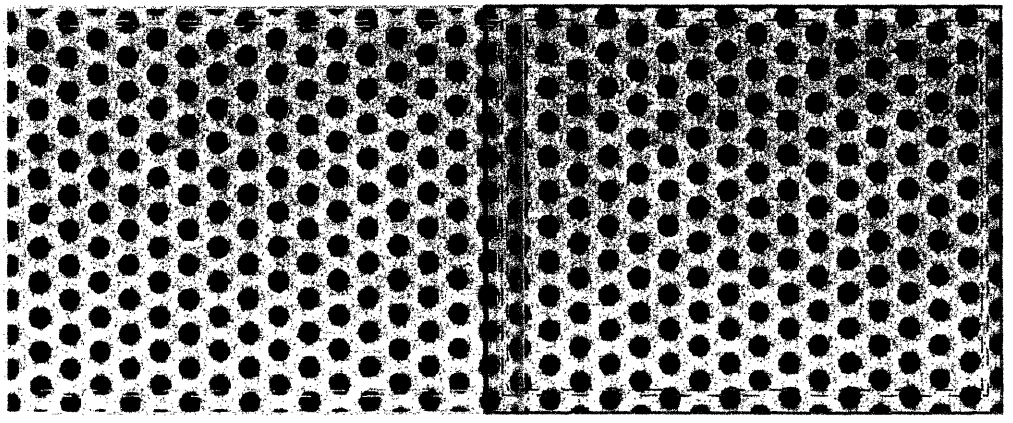

Figure 4-6: Illustration of typical overlap between frames.

The dashed boxes just inside the "ignore borders" define "duplication borders." Any feature with a centroid lying between the duplication border and the ignore border is likely to be captured in multiple image frames ("duplicated" in the data set). Such features are tagged as possible duplicates during image acquisition. These features are then filtered during data processing, and duplicate features are eliminated from the data set. The filtering procedure is described in Section 4.2.4. Tagging potential duplicates at the acquisition stage speeds up processing by reducing the pool of duplicate candidates from the entire data set to a much smaller subset.

The nominal hole diameter (call it $\bar{D}$) constrains the width of the ignore border W_I, the width of the overlap W_O, and the width of the duplication border W_D (defined as the distance between the ignore border and the duplication border). If the stages could be perfectly positioned and no hole diameter exceeded $\bar{D}$, then these widths

[12]The MATLAB Image Processing Toolbox function `clearborder` eliminates features connected to the border of a binary image. The procedure described here was found to be much faster than using `clearborder` on each image.

could be set to

$$\begin{aligned} W_I &= \bar{D}/2 \\ W_O &= 2W_I \\ W_D &= 0 \end{aligned} \tag{4.1}$$

so that no hole would be captured in more than one frame.

In practice, the stages cannot be perfectly positioned, and some hole diameters do exceed $\bar{D}$. To accommodate these non-idealities, the widths must be selected such that

$$\begin{aligned} W_I &> \bar{D}/2 \\ W_0 &> 2W_I \\ W_D &> (W_0 - W_I)/2\,. \end{aligned} \tag{4.2}$$

For simplicity the nominal copper hole diameter is usually treated as $\bar{D}$ for both copper and Kapton diameter scans. If $\bar{D} = 100$ μm, then widths of 75 μm, 155 μm, and 10 μm might be chosen for W_I, W_O, and W_D respectively.

4.2.3.2 Feature Extraction

The centroids and diameters of every hole (or other high-contrast feature) in each frame must be extracted from the initial grayscale image. While edge-detection might seem an obvious means of extracting this data, early attempts at such an implementation were found to be much too slow (on the order of a few seconds per frame at 3.5 μm/pixel). The method ultimately employed in GEMScan first converts each image to binary form (so that each pixel is either pure black or pure white) and then computes the centroids and diameters[13] of the clusters of white pixels.

Figure 4-7 illustrates the progression from grayscale images to binary images to

[13]The computed diameter is actually an "equivalent diameter" based on the area of the pixel cluster.

centroid and diameter data. The upper three sub-figures depict this progression for backlit Kapton holes, while the lower three do the same for copper holes under front illumination. Note that holes near the frame perimeter have been ignored and do not appear in the rightmost sub-figures.

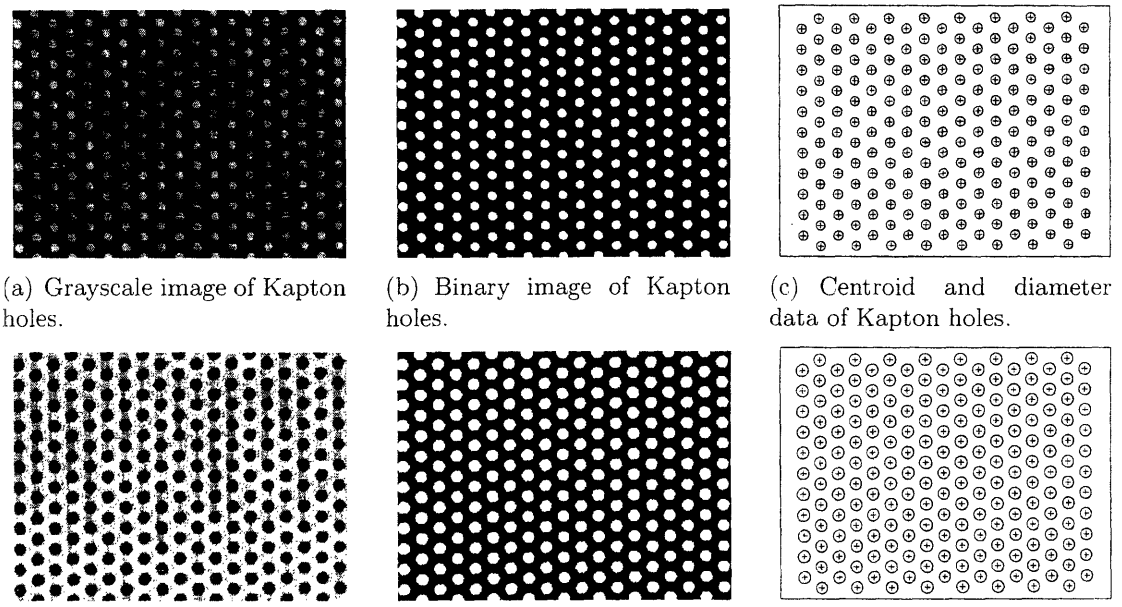

(a) Grayscale image of Kapton holes.

(b) Binary image of Kapton holes.

(c) Centroid and diameter data of Kapton holes.

(d) Grayscale image of copper holes.

(e) Binary image of copper holes.

(f) Centroid and diameter data of copper holes

Figure 4-7: Progression from grayscale images to binary images to centroid and diameter data for Kapton and copper holes.

The MATLAB Image Processing Toolbox contains built-in functions designed specifically to implement this type of feature extraction. The data can be obtained using the following command sequence:

```
binaryImage = im2bw(grayscaleImage, grayThreshold);
labelMatrix = bwlabel(binaryImage);
featureData = regionprops(labelMatrix, 'Centroid', ...
    'EquivDiameter');
```

In this code segment, `grayscaleImage` is the initial image acquired by the camera, and `grayThreshold` is the fractional intensity value a pixel must exceed to be considered white. The selection of threshold values is discussed in Section 4.3.3.

The code listed above works fine for images of Kapton holes, but two minor

additions are necessary for images of copper holes. As can be seen in Figure 4-7(d), copper holes appear black against a lighter background. The label matrix must therefore be formed from the logical inverse of the binary image. Additionally, small copper discolorations can appear as black specks (perhaps only a few pixels in area) against the light gray of the normal copper surface. To prevent these very small discolorations from being treated as foil defects during processing, a user-settable minimum feature size parameter can be set to a nonzero value to instruct GEMScan to ignore all high-contrast features smaller than the specified size.

4.2.4 Data Processing

After acquisition the data consists of just three vectors (X coordinates, Y coordinates, and diameters) each roughly 600,000 elements long. The vector elements are in the order in which the data was acquired. Making sense of all this information to locate foil defects requires the processing algorithms described in this section.

4.2.4.1 Centroid Triangulation

Several possible approaches for locating defects were considered before developing the extremely simple but robust method that was ultimately selected. It is useful to consider these other possible techniques to understand the advantages of the one that was actually implemented.

One obvious method would involve completely predefining the expected hole pattern and comparing the actual acquired feature centroids with the expected hole coordinates. This approach is unsatisfactory for two reasons. Firstly, it requires detailed knowledge of the hole layout to be input into the software. The user must know exactly how many rows of holes are in the foil, the precise hole pitch, whether the first hole of the second row is to the left or right of the first hole of the first row, etc. Even if this information is well known for one particular foil, a user may not know such details about a foil from a different manufacturer. Secondly, this method is not robust to thermal expansion/contraction or stretching of the foil. A 10 cm wide GEM

with a nominal hole pitch of 140 μm contains more than 800 rows of more than 700 holes each. A deviation from the expected hole pitch of just 0.1 μm would cause holes on the edge of the GEM opposite the pattern origin to lie 70 μm (half the nominal pitch) from where they were expected. Thousands of false pattern violations would result.

A pattern-matching technique is another possibility. MATLAB provides a number of functions which could be used to implement a matching algorithm perhaps based on cross correlations or even neural networks. Such algorithms are routinely used in character recognition applications. Since the GEM hole pattern is so simple, however, the computational overhead of these very robust methods seemed excessive.

The approach ultimately used for the GEM scanner exploits the extreme regularity of the GEM hole pattern. A Delaunay triangulation of the centroids is computed. Such a triangulation is defined such that the circumscribed circle of each triangle formed from the input set of coordinates encloses no data points [30]. The actual computation is performed using the MATLAB built-in function `delaunay`.

Triangles associated with defects are very different from triangles associated with regions free of defects. Figure 4-8 illustrates the differences between the Delaunay triangulations of a region of a hexagonal GEM that contains no defects and a region that contains multiple defects. As can be seen in Figure 4-8(a), every Delaunay triangle in a region without defects is equilateral with side length equal to the hole pitch. The boxed area labeled A in Figure 4-8(b) is missing 3 holes, while the areas labeled B and C contain high-contrast material between holes. The area labeled D contains 2 smaller features at a location where a hole should appear. This type of defect might be caused by a piece of debris partially filling a hole. In all of the boxed regions in this figure, the pattern of equilateral triangles is broken. Foil defects due to pattern violations can thus be located simply by finding triangles that have at least one side length that deviates from the designed hole pitch beyond some tolerance.[14]

This simple property of Delaunay triangulations forms the basis of GEMScan's

[14]Though this discussion has assumed a hexagonal pattern, the same technique can be applied to a square pattern. The Delaunay triangles are then isosceles. The scanner software was programmed to handle GEMs with either hexagonal or square hole patterns.

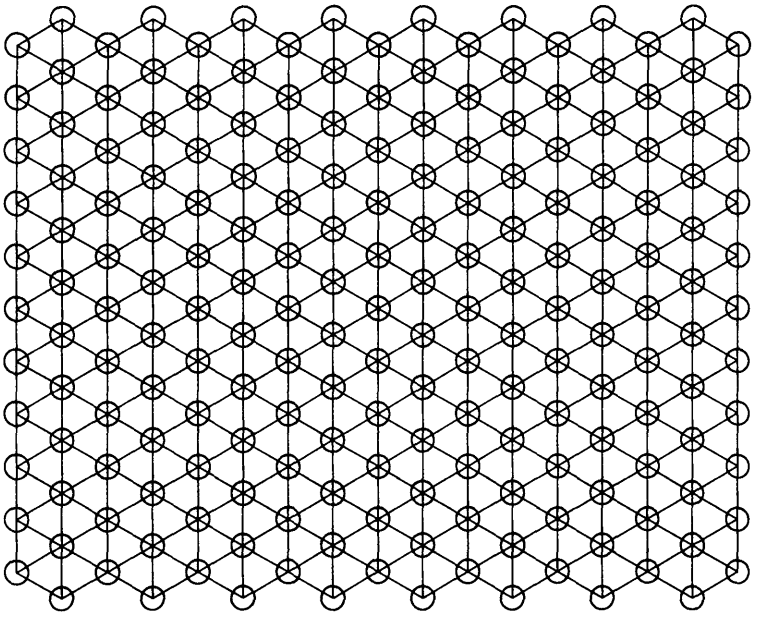

(a) Triangulation of region free of violations.

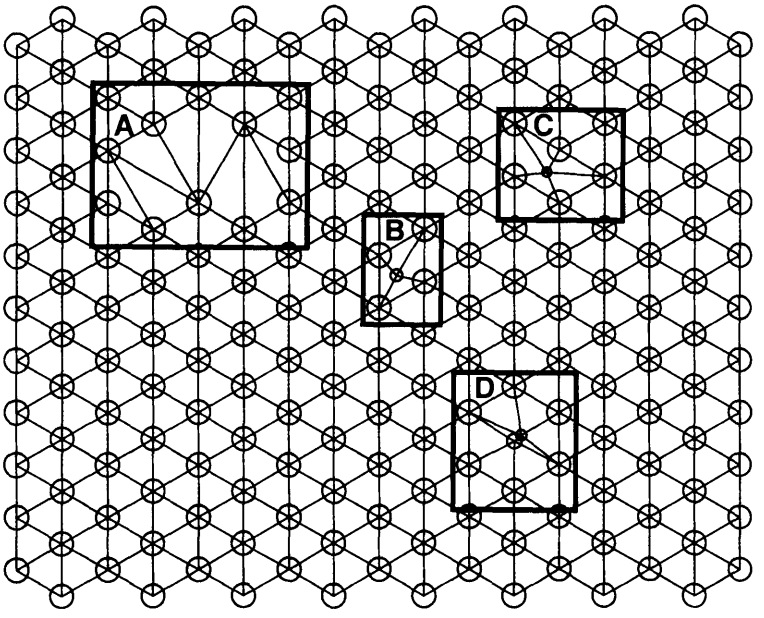

(b) Triangulation of region containing multiple violations.

Figure 4-8: Illustration of differences between triangulations of GEM regions with and without violations.

defect localization algorithm, which can be summarized by the following sequence of steps:

1. **Filtering Duplicate Data Points:** As was discussed in Section 4.2.3.1, the finite overlap between image frames results in multiple occurrences of some features in the data set. Possible duplicate features were tagged during acquisition. The user defines a coincidence radius r_c, typically on the order of a few microns. If a set of tagged features has centroids that can be enclosed by a circle of radius r_c, then that set of features is removed from the data set and is replaced by a single feature with a centroid and a diameter equal to the mean centroid and the mean diameter of the original set.

2. **Computing the Triangulation:** The Delaunay triangulation of the filtered centroids is computed. MATLAB stores the triangulation as a 3-column matrix in which each row contains indices into the centroid X and Y coordinate vectors corresponding to a single triangle's vertices.

3. **Filtering Border Triangles:** Triangles with all three vertices belonging to holes on the border of the GEM deviate from the equilateral pattern. These triangles must be filtered from the triangle matrix to prevent them from being treated as the results of actual foil defects.

4. **Identifying Violation Triangles:** A list of all "violation triangles" associated with hole pattern irregularities is generated. The user defines the designed hole pitch P and a corresponding tolerance σ_P. Any triangle with side lengths a, b, and c that do not satisfy

$$(a-P)^2 + (b-P)^2 + (c-P)^2 < \sigma_P^2 \tag{4.3}$$

is considered a violation triangle. Additionally, a triangle which satisfies Eq. 4.3 but shares all three of its vertices with triangles that do not satisfy Eq. 4.3 is also considered a violation triangle.

5. **Clustering Violation Triangles:** As can be seen in Figure 4-8(b), violation triangles usually occur in groups. GEMScan sorts the full list of violation triangles into clusters of adjacent triangles (where *adjacent* is defined as the sharing of a side). Each hole pattern irregularity is then associated with a single region bounded by the vertices of the outermost triangles of the associated cluster.

4.2.4.2 Violation Classification

The final stage of data processing is the generation of a list of hole size and pattern violations classified on the basis of the geometry of the violations.[15] The goal of this classification is to associate every location where a well-formed hole is expected but not found with a single violation of a particular type. Features located between expected hole locations are also classified. It should be emphasized that this classification cannot automatically discern the underlying cause of a violation (e.g. a piece of dust or an incomplete etch). This method can, however, tell the user how many hole locations are affected by abnormalities, and some geometrical categories are closely correlated with certain underlying causes.

Each violation is placed in one of six geometrical categories. The category definitions require a number of variables. Let the designed hole diameter and pitch be given by D and P with corresponding tolerances given by σ_D and σ_P. Let the centroid coordinates and the diameter of the i^{th} captured feature be given by x_i, y_i, and d_i.

- **Missing Hole:** Absence of a hole at a location where one is expected based on the hole pattern.[16] A hole at the expected location (x_e, y_e) is missing only if

$$\sqrt{(x_e - x_i)^2 + (y_e - y_i)^2} + \frac{d_i}{2} > \frac{D + \sigma_D}{2} \tag{4.4}$$

[15] While pattern violations are, by construction, associated with clusters of violation triangles, hole size violations (holes with diameters above or below a user-settable value beyond a specified tolerance) can occur anywhere on the GEM.

[16] This discussion of "expected" hole locations might give the impression that a predefined pattern like that described at the beginning of Section 4.2.4 is being used. GEMScan actually computes global pattern parameters (both pitch and pattern rotation angle) by averaging over the acquired centroid data. A small patch of an ideal hole pattern with these parameters is then fit through the centroids of holes along the perimeter of a particular cluster of violation triangles. The "expected" hole locations are thus only locally defined, and the problems of a fully predefined pattern are avoided.

for all i. That is, a missing hole occurs when the captured feature nearest an expected hole location extends beyond a circular region of diameter $D + \sigma_D$ centered at the expected point.

- **Non-Hole:** Any feature located between expected hole locations or an oversize feature located near a shifted, split, or normal hole. For feature i to be considered a non-hole, the inequality in Eq. 4.4 must hold for all expected hole positions (x_e, y_e). Feature i must also satisfy one of the following conditions:
  - The distance between feature i and the nearest expected hole location is greater than σ_P.
  - The distance between feature i and the nearest shifted, split, or normal hole is less than σ_P.

- **Oversize Hole:** Hole found at an expected location but having an oversize diameter. Feature i is oversize if its diameter satisfies

$$d_i - D > \sigma_D \,. \tag{4.5}$$

- **Shifted Hole:** Hole of the correct diameter but displaced from the expected location. Feature i is a shifted hole if

$$\sigma_P < \sqrt{(x_e - x_i)^2 + (y_e - y_i)^2} < \frac{D + \sigma_D}{2} - \frac{d_i}{2}$$

$$\text{and } |d_i - D| < \sigma_D \,, \tag{4.6}$$

  where (x_e, y_e) is the expected hole location nearest feature i.

- **Split Hole:** Multiple features located in an area a hole is expected to occupy. At least two features must satisfy

$$\sqrt{(x_e - x_i)^2 + (y_e - y_i)^2} + \frac{d_i}{2} < \frac{D + \sigma_D}{2} \,, \tag{4.7}$$

where the expected hole location (x_e, y_e) is that expected location which is nearest the centroids of all constituent features. A split hole typically occurs when debris partially fills a hole and creates the appearance of multiple high-contrast features.

- **Undersize Hole:** Hole found at an expected location but having an undersize diameter. Feature i is undersize if its diameter satisfies

$$D - d_i > \sigma_D \,. \tag{4.8}$$

4.3 Scanner Setup and Calibration

Before a GEM can be scanned, the apparatus must be set up and calibrated. This section describes the calibration of the camera-stage alignment, the selection of scan region boundaries, and the adjustment of the imaging components for optimal diameter measurement accuracy and repeatability. The section concludes with a summary of measurement errors.

4.3.1 Camera-Stage Alignment

The stage-x and stage-y coordinates define a global coordinate system for the scanner. The centroid of a hole in an image captured by the video camera is known in terms of vertical and horizontal pixel coordinates. Relating pixel coordinates to stage coordinates requires knowledge of two parameters: a linear scaling factor A in units of μm/pixel and a rotation angle θ between the camera axes and the stage axes. Both parameters are determined through the following two point calibration (the geometry is shown schematically in Figure 4-9):

1. The stages are positioned to place a prominent GEM feature (usually a corner hole) in one quadrant of the camera's field of view.

2. Using the mouse to define a rectangular region on the GEMScan image display,

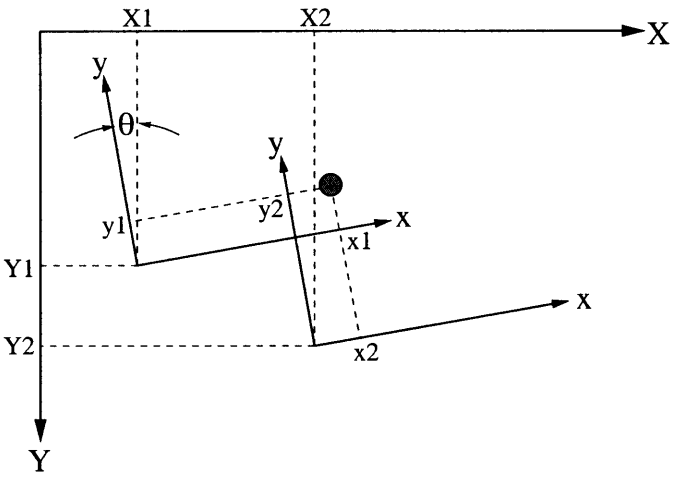

Figure 4-9: Schematic of camera-stage alignment geometry.

the user selects the feature. That portion of the image is converted to binary, and the centroid of the feature is computed.

3. Both the current stage position (X_1, Y_1) and the pixel coordinates of the selected feature's centroid (x_1, y_1) are saved to memory.

4. The stages are repositioned to place the same GEM feature in the diagonally opposite quadrant of the camera's field of view.

5. Again, the user selects the feature, and its centroid is computed.

6. Both the new stage position (X_2, Y_2) and the new pixel coordinates of the selected feature's centroid (x_2, y_2) are saved to memory.

7. With the assumption that the camera axes and stage axes are nearly aligned, θ can be approximated as a small angle and the following expressions for A and θ can be found:

$$A \approx \frac{\Delta Y \Delta y - \Delta X \Delta x}{(\Delta x)^2 + (\Delta y)^2}$$
$$\theta \approx \frac{A\Delta y - \Delta Y}{A \Delta x}, \tag{4.9}$$

where $\Delta X = X_2 - X_1$, and ΔY, Δx, and Δy are defined similarly.

The entire calibration procedure takes only a few seconds for the user to perform. The software does all calculations internally, so that the user need only twice position the stages and select a feature as described. Once the calibration is completed, all measurements in the current scan session use the coordinate transformation defined by the calculated values of A and θ.

The uncertainty in hole positions and diameters introduced by this calibration is very small as long as the positions of the prominent GEM feature in Steps 1 and 4 are as close as possible to two diagonally opposite corners of the camera's field of view. For a nominal magnification of 3.5 μm/pixel, the uncertainty in A is ± 0.0014 μm/pixel. The uncertainties in a 140 μm pitch and a 100 μm diameter are then ± 0.06 μm and ± 0.04 μm respectively. Such uncertainties are insignificant relative to the other sources of error described later in this section.

4.3.2 Scan Boundary Selection

GEMScan requires a user to select the boundary of the region of the GEM to be scanned (usually the GEM's entire active area). The user simply positions the GEM so that its upper-left corner is in the camera's field of view as shown in Figure 4-10. Using the mouse the user selects the a point on the GEMScan image display roughly at the intersection of a line joining the upper row of holes and a line joining the leftmost column of holes. GEMScan fits the centroids of holes in the upper row (between the two dashed horizontal lines in the figure) to one line (the solid, roughly horizontal line in the figure) and performs a similar fit for holes in the leftmost column to find another line (the solid, roughly vertical line in the figure). The intersection of these fitted lines is set as the upper-left corner of the scan boundary. The user repeats this process for the lower-left and lower-right corners, and GEMScan infers the upper-right corner coordinates from symmetry.

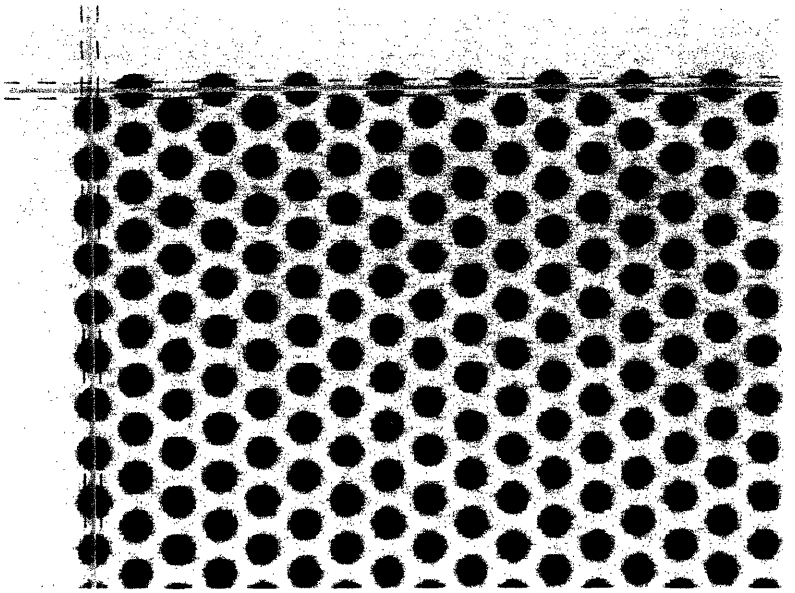

Figure 4-10: Illustration of upper left boundary point selection.

4.3.3 Hole Diameter Calibration

Measuring the diameter of any backlit hole is complicated by diffraction of light around the hole's perimeter. Figure 4-11 shows the variation in the measured Kapton diameter of a single GEM hole as a function of backlight intensity. To avoid a systematic overestimate of Kapton diameters, the backlight must be dimmed to the lowest intensity at which features can still be reliably extracted.

Measurements of both Kapton and copper holes are also affected by changes in the camera exposure, contrast, and gain settings as well as the gray threshold (for grayscale-to-binary image conversion). With so many degrees of freedom, the following systematic calibration method is necessary to obtain accurate, repeatable diameter measurements:

1. The zoom is set for a magnification 3–4 times the level typically used for scanning, and the light intensity and camera settings are adjusted to produce a Kapton hole image of adequate contrast.

2. A best estimate of the actual Kapton diameters of a few prominent GEM holes (usually at the corners) is obtained at high magnification. The GEMScan in-

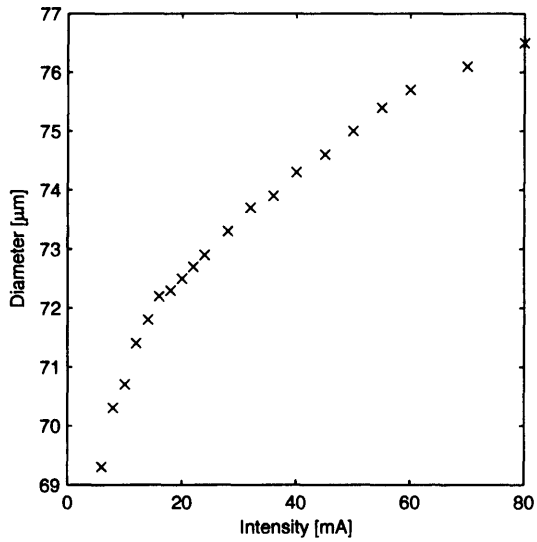

Figure 4-11: Measured Kapton diameter of GEM corner hole as function of backlight intensity.

dividual feature measurement tool displays a highlight box with side lengths equal to the measured diameter at the centroid of the feature being measured. The user adjusts the gray threshold until this highlight box coincides with the apparent perimeter of the hole as seen in the grayscale image in the GEMScan display.

The dependence of both Kapton and copper diameter measurements upon the gray threshold is plotted in Figure 4-12. In each plot, the points lying between the vertical dashed lines correspond to thresholds for which the measure tool highlight box and the apparent perimeter of the hole were visually indistinguishable. As can be seen from these plots, the uncertainty in the diameters is roughly ± 2 μm.

3. Steps 1 and 2 are repeated for copper holes.

4. The magnification is returned to the normal level (roughly 3.5 μm/pixel), and the light intensity and camera settings are again adjusted to produce a Kapton hole image of adequate contrast.

5. The same set of holes measured in Step 2 are remeasured at normal magnifica-

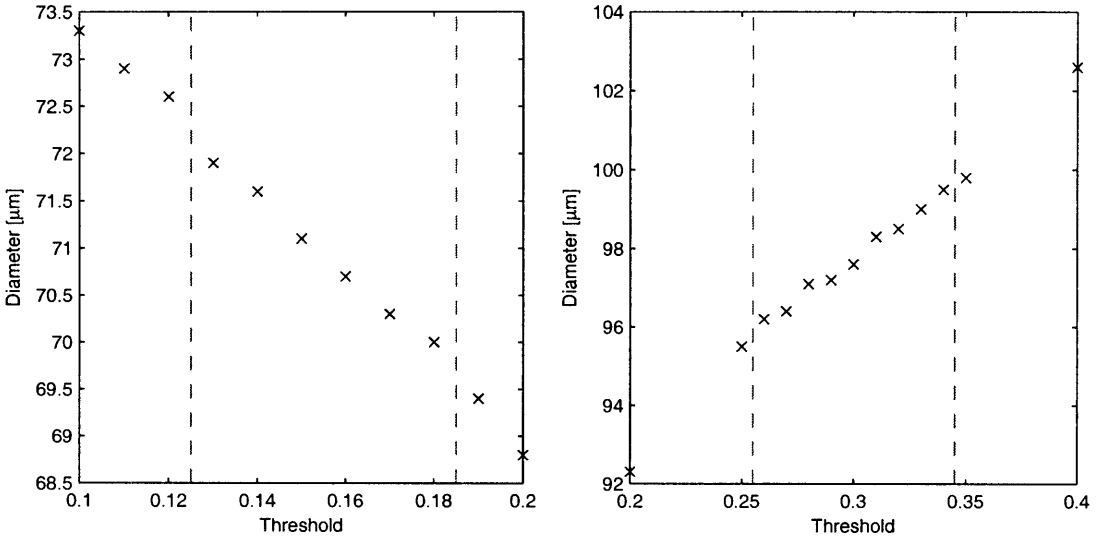

Figure 4-12: Measured Kapton (a) and copper (b) diameters of GEM corner hole as functions of gray threshold.

tion for a range of gray threshold values.

6. For each hole, the threshold at which the low magnification diameter equals the high magnification diameter (interpolating between data points) is recorded. The mean of these values is taken as the optimal gray threshold.

7. Steps 4–6 are repeated for copper holes.

This calibration is admittedly tedious, but it need not be performed before every scan. Recalibration should not be necessary as long as the lighting intensities are stable, the zoom setting is not changed, and the overall coloration of the foils being scanned is constant (i.e. the copper of different GEMs does not show varying degrees of oxidation).

4.3.4 Error Analysis

Knowledge of the scanner components and calibration procedures permits an estimate of the systematic and random errors in measured hole diameters and positions.

The systematic diameter error is due to imperfection in both the camera-stage

alignment calibration and the hole diameter calibration. The camera-stage alignment component is only ± 0.04 μm for a nominally 100 μm diameter. The hole diameter calibration component of ± 2 μm can thus be treated as the total systematic diameter error.

A significant source of random diameter error is the finite resolution of the camera. As was mentioned in Section 4.2.3.2, diameters are actually calculated from the areas of white pixel clusters in binary images. For a magnification of 3.5 μm/pixel, the area of a single pixel is $\Delta A = 12.25$ μm^2. The corresponding diameter resolution is

$$\Delta d \approx \frac{2\Delta A}{\pi d}, \tag{4.10}$$

for a hole of nominal diameter d. Δd is 0.16 μm and 0.08 μm for diameters of 50 μm and 100 μm respectively.

Small variations in lighting intensity over the camera's field of view as well as any uncertainty in the camera-stage alignment parameter θ introduce quasi-random error into the diameter measurements. That is, these non-idealities cause the measured diameter of a particular hole to vary with the hole's relative position in the camera's field of view.

Table 4.1: Variation over image frame in measured diameter and position of GEM corner hole.

	Kapton			Copper		
	d [μm]	x [μm]	y [μm]	d [μm]	x [μm]	y [μm]
C	71.0	0.0	0.0	97.8	0.0	0.0
UL	70.7	0.5	-0.5	98.5	0.3	0.3
LL	70.5	-0.2	1.2	98.4	-0.3	0.1
LR	71.0	-0.1	0.3	98.1	0.0	0.3
UR	70.3	-0.5	0.1	98.5	0.5	0.1
StDev	0.3	0.4	0.6	0.3	0.3	0.1

Table 4.1 shows the variation in diameter and position measurements of a single GEM hole taken at different locations in the camera's field of view with the scanner operating in either Kapton or copper hole mode. C indicates the center of the field,

UL indicates the upper-left corner, and the remaining abbreviations indicate the other three corners. The position coordinates were normalized to the center field values. As shown in the table, the standard deviation of these diameter measurements is 0.3 μm. This value includes contributions from the finite camera resolution, lighting intensity variation, and uncertainty in θ and provides a reasonable estimate of the total random diameter error.

While the absolute error in positions of the GEM holes is not critical, random error in relative feature positions is important, since pattern violations are identified primarily on the basis of the distances between adjacent features. This error is due to both the finite camera resolution as well as the limited stage encoder resolutions (0.5 μm and 1.0 μm for stage-x and stage-y respectively). Table 4.1 suggests a random position error on the order of 0.5 μm. Hole pitch measurements are used in Section 5.1.3 to improve this estimate.

Chapter 5

Scan Results

This chapter serves the dual purpose of both demonstrating the capabilities of the quality control scanner described in the previous chapter and quantifying the quality and variation of Tech-Etch GEMs.

Two Tech-Etch GEMs were selected for complete characterization using the scanner. These particular GEMs were classified as "good" based on macroscopic testing by S. Hertel [31]. Both foils (labeled B12 and B15) were manufactured in November of 2004 and were stretched prior to scanning. A high voltage was applied across each foil in a dry nitrogen atmosphere and the leakage currents were measured. For an applied voltage of 500 V, currents of 1.2 nA and 6.1 nA were recorded for B12 and B15 respectively.

The first section of this chapter describes the results of geometry measurements and estimates of the impact of diameter variations on gain, and the second shows the nature and extent of pattern and hole-size violations located by the scanner.

5.1 Geometry Measurements

This section presents diameter and pitch measurements in the same graphical format automatically generated by GEMScan. The estimated effect of diameter inhomogeneity on effective GEM gain is also calculated. Note that throughout this chapter to save page area, only plots of measurements from one side of B12 and one side of B15

will be shown. Very similar results were obtained for each foil's opposite side.

5.1.1 Hole Diameter

Histograms of Kapton and copper hole diameters for both GEMs are shown in Figure 5-1. As indicated in these plots, the Kapton diameters averaged roughly 50 μm, while the copper diameters averaged about 80 μm. The mean Kapton and copper diameters for B15 were 4 μm larger than the corresponding diameters for B12. Recall from Section 4.3.4, that these diameter measurements have systematic and random errors of ± 2 μm and ± 0.3 μm respectively.

Color plots indicating the spatial homogeneity of Kapton and copper hole diameters are shown for both GEMs in Figures 5-2 and 5-3. Each colored square patch in the plots represents a 2×2 μm region of the respective GEM. The color of the square patch indicates the average Kapton or copper hole diameter within the region. Two interesting characteristics are visible in these plots. Firstly, the small standard deviations of approximately 2 μm observed in the global diameter distributions (Figure 5-1) obscure the considerably larger local diameter variations among various regions of the GEMs. The contributions of these variations to gain inhomogeneity is discussed in Section 5.1.2. Secondly, the spatial distribution of diameters for B12 is very different from the distribution for B15. While larger holes in B15 occur along the GEM's perimeter, larger and smaller holes in B12 are distributed more randomly. This variation might be caused by differences in acid agitation during etching.

5.1.2 Gain Effects

As discussed in Chapter 2, the effective GEM gain G_{eff} is very sensitive to changes in hole diameter. The impact of local copper diameter variations (apparent in Figures 5-2(b) and 5-3(b)) on gain can be estimated from measurements of the effective gains of CERN GEMs published by J. Benlloch et al. [18]. The authors plotted the measured gains (at $\Delta V_{\text{GEM}} = 500$ V in Ar-CO_2 70-30) of detectors built with nine different double-conical GEMs with copper diameters D ranging from 45 μm to 140 μm

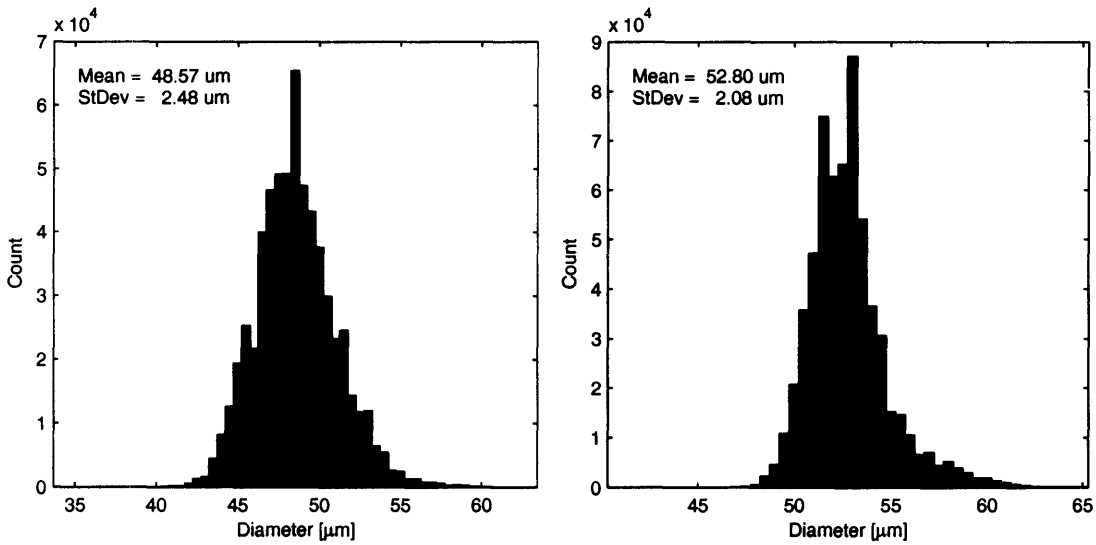

(a) Kapton diameters, B12.

(b) Kapton diameters, B15.

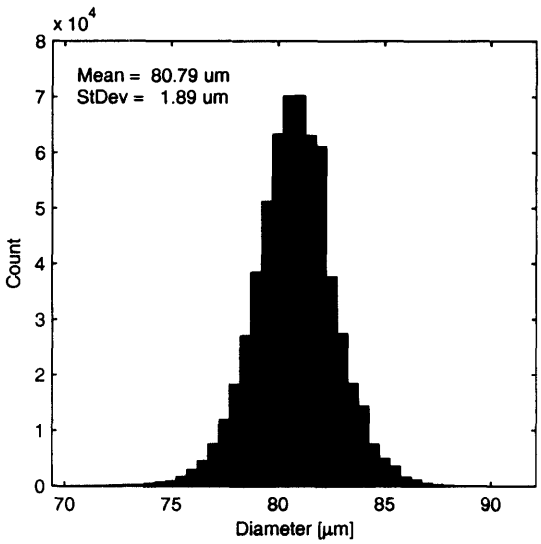

(c) Copper diameters, B12.

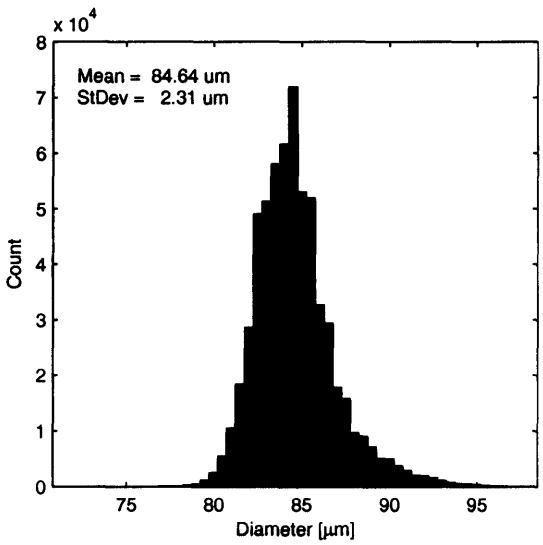

(d) Copper diameters, B15.

Figure 5-1: Histograms of Kapton and copper hole diameters for two Tech-Etch GEMs.

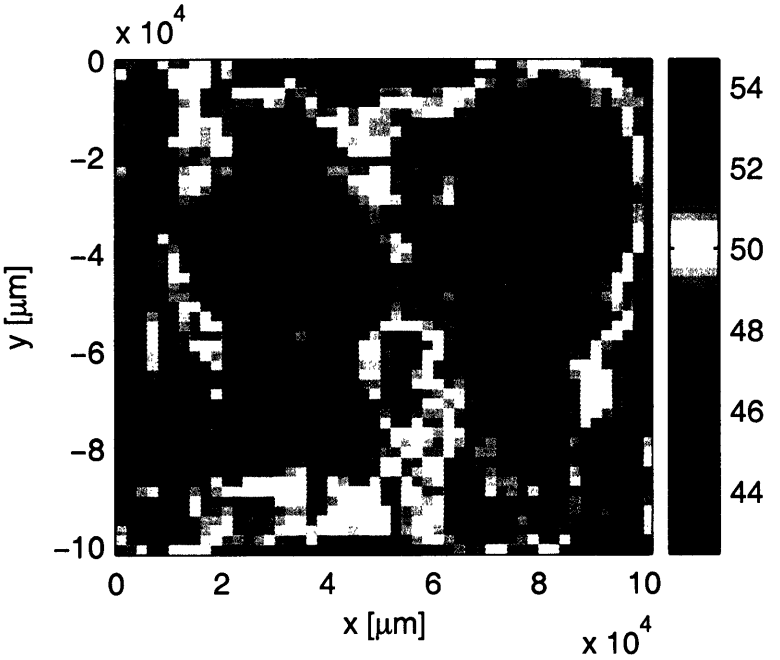

(a) Kapton diameters, B12.

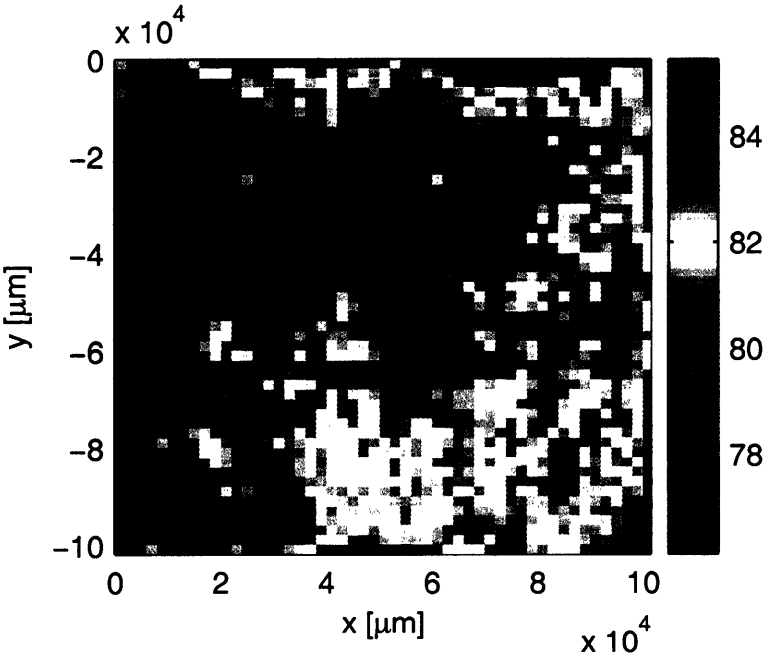

(b) Copper diameters, B12.

Figure 5-2: Kapton (a) and copper (b) hole diameters [μm] averaged over 4 μm^2 for Tech-Etch GEM B12.

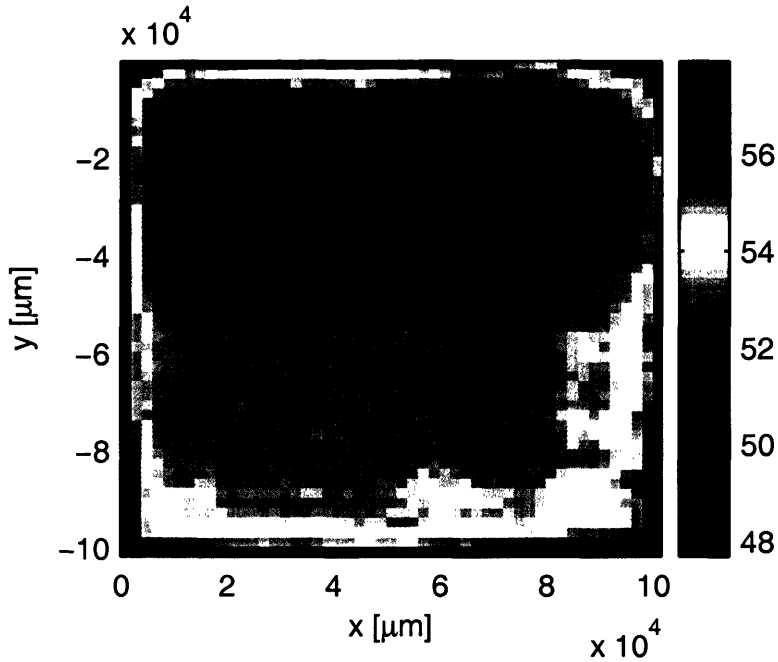

(a) Kapton diameters, B15.

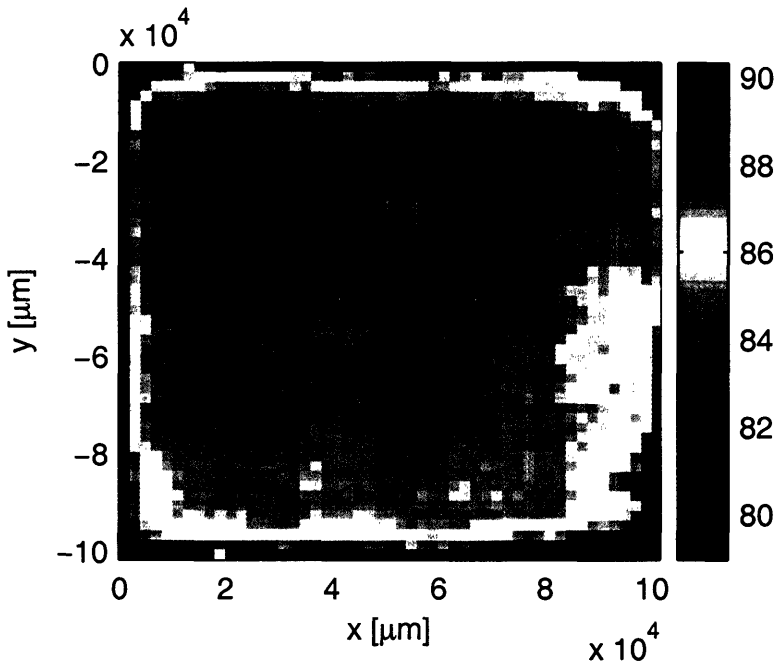

(b) Copper diameters, B15.

Figure 5-3: Kapton (a) and copper (b) hole diameters [μm] averaged over 4 μm^2 for Tech-Etch GEM B15.

(see Figure 1-6). This plot showed that G_{eff} increased exponentially with decreasing copper diameter until saturating for $D < 70$ μm. Measurements for $D \geq 70$ μm in the published plot were fit to the equation,

$$\log G_{\text{eff}} = -(0.022 \pm 0.003)D + (4.1 \pm 0.3)\,. \tag{5.1}$$

Figures 5-2 and 5-3 show that some areas of each Tech-Etch foil have local mean diameters more than 2σ above or below the global mean. The measured global mean copper diameter $\bar{D}$ as well as $\bar{D} \pm 2\sigma_D$ for B12 and B15 were substituted into Eq. 5.1 to find the estimated variation in effective gain listed in Table 5.1. It should be noted that the roughly 10% uncertainties in the fitted parameters in Eq. 5.1 lead to absolute gain uncertainties of the same order as the gains themselves. This error is primarily due to the Benlloch group's small sample size and diameter uncertainties of ± 5 μm. Only relative gain variations, however, are of interest here.

Table 5.1: Estimated effect of diameter variation on effective gain of two Tech-Etch GEMs.

	B12		B15	
	D [μm]	G_{eff}	D [μm]	G_{eff}
$\bar{D} - 2\sigma_D$	77.0	252	80.0	216
$\bar{D}$	80.8	207	84.6	171
$\bar{D} + 2\sigma_D$	84.6	171	89.2	135

Table 5.1 suggests local gain variations for the two Tech-Etch GEMs of about $\pm 20\%$.

5.1.3 Hole Pitch

While hole pitch does not critically affect gain, a measurement of pitch requires no additional scan time and provides a simple way of placing an upper limit on the random error in the scanner's position measurements. Histograms of hole pitch for both GEMs are shown in Figure 5-4. The mean pitch indicated in both plots lies within a fraction of a micron from the designed value of 140 μm. These histograms are almost perfectly Gaussian due to the extremely large sample sizes (600,000 holes correspond

to more than 1,000,000 pitch measurements). Additionally, pitch is defined during manufacture by the photo-resist mask. Unlike the case of hole diameters, one does not expect pitch to vary systematically over the GEM surface assuming even foil stretching and proper mask production. The standard deviations σ_{meas} of the pitch measurements incorporate the random positioning errors of both the scanner σ_{scan} and the foil manufacturing process σ_{manuf}

$$\sigma_{\text{meas}} = \sqrt{\sigma_{\text{scan}}^2 + \sigma_{\text{manuf}}^2}. \tag{5.2}$$

Even without knowing σ_{manuf}, the scanner's random positioning error must be less than ~ 0.6 μm, in agreement with the estimate in Section 4.3.4.

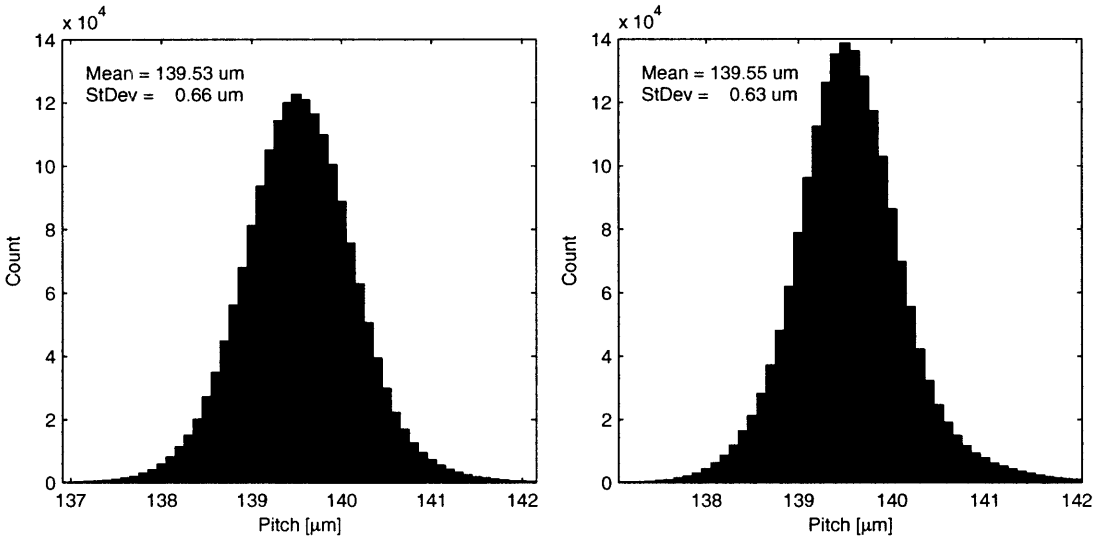

(a) B12 (b) B15

Figure 5-4: Histograms of hole pitch for two Tech-Etch GEMs.

5.2 Foil Defects

Despite the promising indications of the macroscopic measurements, a number of defects were found in each GEM. Because these scans were not conducted in a clean room, a large portion of the hole size and pattern violations located by the scanner were due to dust and debris. The spatial distributions of violations are plotted ac-

cording to geometric classification for Kapton and copper hole scans in Figure 5-5. As is readily visible in these plots, the most common violation types in Kapton hole scans are not the same as those in copper hole scans. With a GEM illuminated with the backlight, only defects that occur within a hole can be imaged. Pieces of debris on either side of the GEM, for instance, cause numerous missing, shifted, and split hole violations. With a GEM illuminated with the ring light, however, defects between the holes are visible. Pieces of debris on the front side of the GEM can overlap one or more holes and create the appearance of large, misshapen high-contrast features, which GEMScan classifies as missing holes and non-hole violations.

Images of typical violations located by the scanner are shown in Figure 5-6. For illustrative purposes, these microphotographs were taken at roughly four times the normal scan magnification. The small piece of dust in the hole in Figure 5-6(a) would cause a split hole violation during a backlight scan, while the larger fibrous debris in Figure 5-6(b) would cause multiple missing holes and non-hole violations during a front-light scan. The copper discoloration seen around the hole in Figure 5-6(c) is typical of foil defects found to affect more than 100 holes on each side of B12 and B15. These discolorations, which might be due to incomplete removal of the acid etchant during manufacture or even unnoticed sparks during leakage current measurement, can only be recognized during front-light scans and cause missing hole, non-hole, and oversize hole violations. Figure 5-6(d) shows several holes around which copper has been removed, possibly by etchant seeping beneath the surrounding mask during manufacture. The dark regions are exposed Kapton. This defect could result in multiple oversize or shifted hole violations during a backlight scan as well as missing holes and non-hole violations during a front-light scan. Figures 5-6(e)–5-6(h) show varying degrees of incomplete etching. These defects would cause undersize and missing hole violations during backlight and front-light scans.

Full violation reviews were performed on both sides of B12 and B15. Table 5.2 summarizes the number of holes affected by various foil defects (sorted into the same categories illustrated in Figure 5-6) in each of the two GEMs. Each column corresponds to a single scan of either copper or Kapton holes on a particular side of a GEM.

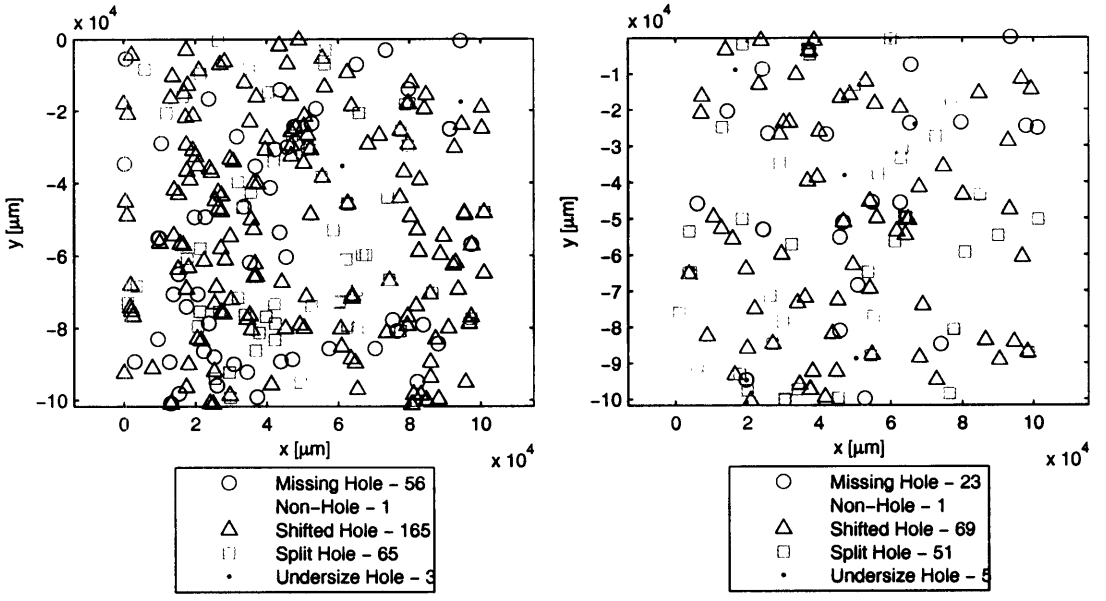

(a) Backlight (Kapton diameter) scan, B12.

(b) Backlight (Kapton diameter) scan, B15.

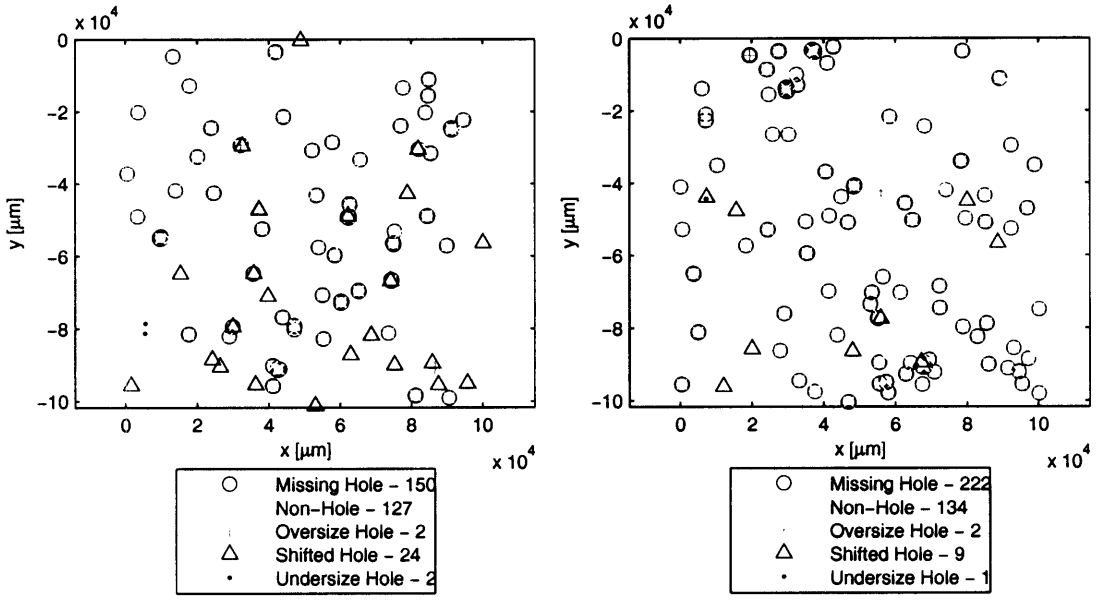

(c) Front-light (copper diameter) scan, B12.

(d) Front-light (copper diameter) scan, B15.

Figure 5-5: Spatial distribution of front-light-scan and backlight-scan feature violations for two Tech-Etch GEMs.

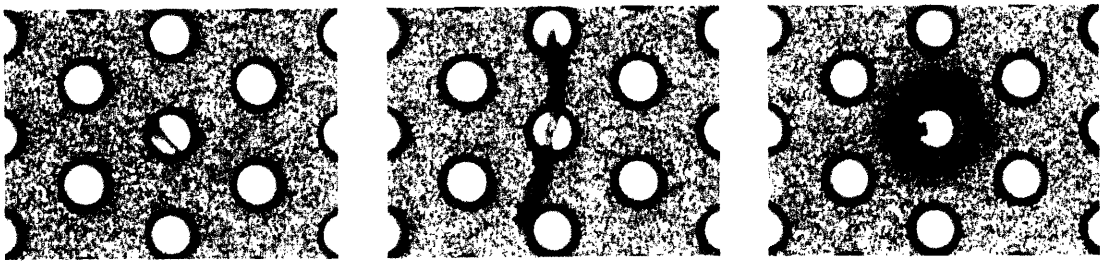

(a) Hole-size debris.

(b) Large debris.

(c) Discoloration.

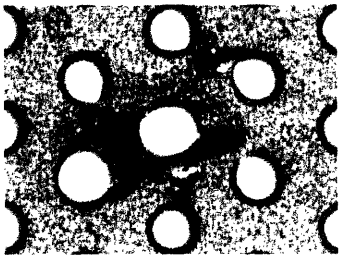

(d) Excess etching.

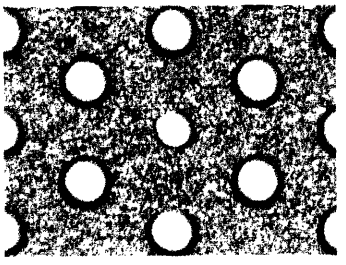

(e) Incomplete copper etching.

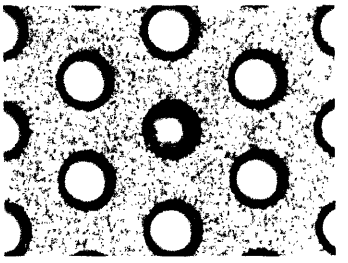

(f) Incomplete Kapton etching.

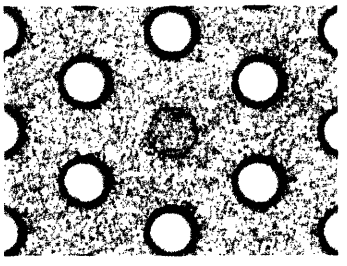

(g) Unetched copper.

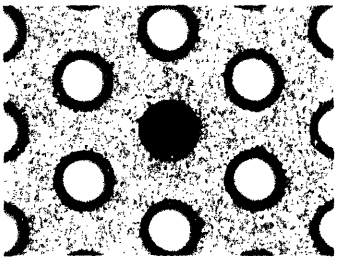

(h) Unetched Kapton.

Figure 5-6: Microphotographs of typical foil defects located during scanning.

While many holes were affected by debris or showed neighboring copper discoloration, only a handful suffered from any degree of incomplete etching.

Table 5.2: Number of hole violations due to various foil defects in two Tech-Etch GEMs.

	B12				B15			
	Side 1		Side 2		Side 1		Side 2	
	Cu	Kap	Cu	Kap	Cu	Kap	Cu	Kap
Debris	64	280	120	277	46	144	51	143
Discoloration	100	0	242	0	179	0	80	0
Excess Etching	8	0	98	0	6	1	3	1
Incomplete Copper Etch	5	3	5	2	3	1	7	4
Incomplete Kapton Etch	0	1	0	0	0	1	0	3
Unetched Copper	1	1	2	2	0	0	0	0
Unetched Kapton	0	4	0	2	0	1	0	1

Chapter 6

Gain Measurement

This chapter describes a preliminary measurement of the gain of a triple GEM detector built with Tech-Etch foils.

Power from a single high voltage supply was distributed to the detector electrodes through a resistor network. Equal potentials ΔV_{GEM} were applied across each of the three GEMs, while the following values were used for the drift, transfer, and induction fields (in V/cm): $E_D = 3.0\Delta V_{\mathrm{GEM}}$, $E_T = 5.6\Delta V_{\mathrm{GEM}}$, and $E_I = 11.1\Delta V_{\mathrm{GEM}}$.

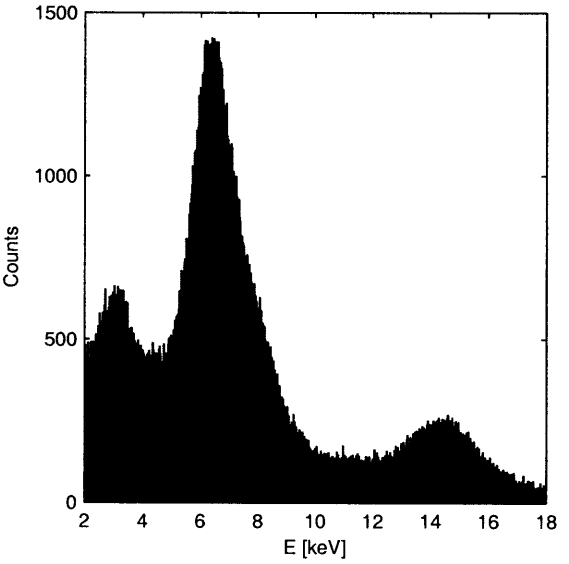

Figure 6-1: ^{57}Fe spectrum.

The detector was filled with P10 (Ar-CH_4 90-10) at 1 atm. Ionization tracks

were produced in the gas volume by x-rays from an ^{57}Fe source. The spectrum of ^{57}Fe (measured by S. Hertel [32]) is shown for illustrative purposes in Figure 6-1. Prominent peaks occur at 6.4 keV and 14.4 keV.

For several values of ΔV_{GEM}, the peak signal voltage as well as the oscilloscope trigger rate were measured over a range of oscilloscope trigger threshold settings. This data is plotted in Figure 6-2. For clarity, error bars have been suppressed. From this data the dependence of the peak signal voltage on ΔV_{GEM} was calculated for several constant values of the trigger rate (each corresponding to a narrow range of energies in the ^{57}Fe spectrum). The results are plotted on a log-linear scale in Figure 6-3. The curves clearly show the expected exponential dependence of gain on ΔV_{GEM}.

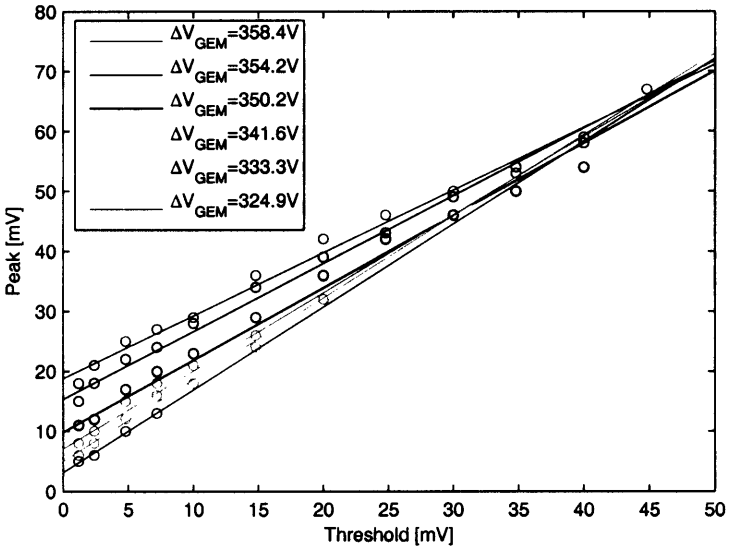

(a) Measured peak signal voltage as function of trigger threshold for several values of ΔV_{GEM}.

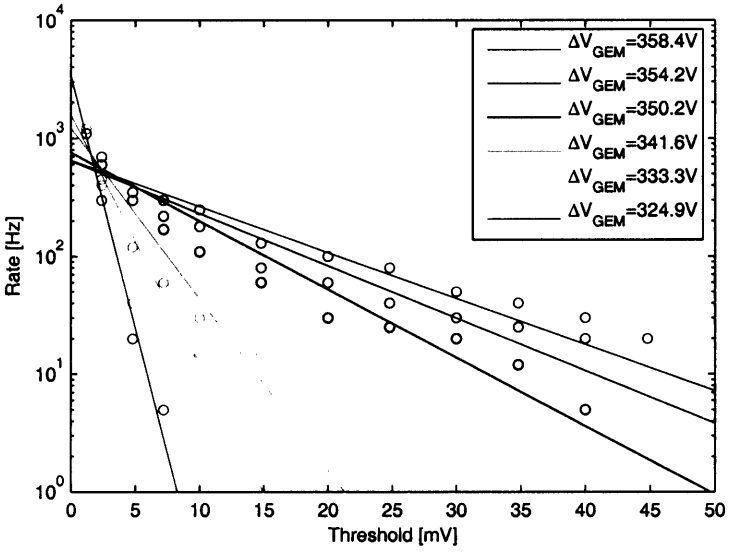

(b) Measured trigger rate as function of trigger threshold for several values of ΔV_{GEM}.

Figure 6-2: Oscilloscope measurements.

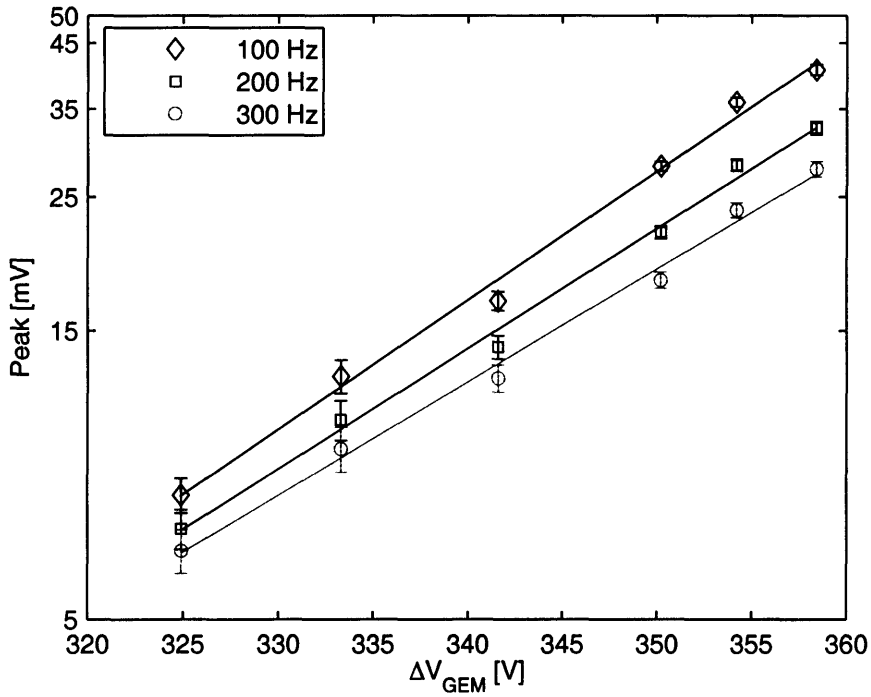

Figure 6-3: Interpolated peak signal voltage as function of ΔV_{GEM} for several trigger rates.

Chapter 7

Conclusions

GEMs are being used in the detectors of a number of new large-scale high-energy experiments and will also be used in the TPC of the future TeV-range ILC. The R&D group of U. Becker in collaboration with Tech-Etch has succeeded in developing quality GEMs. An automated scanner for GEM quality control has been constructed and successfully tested on Tech-Etch GEMs. The machine is capable of measuring hole diameters and locating foil imperfections and debris while examining each of roughly 600,000 holes in a single 30 minute scan. Scans of Tech-Etch GEMs have shown the foils to be largely free of etching defects, but hole diameter variations in a given GEM may be large enough to create a gain inhomogeneity of approximately $\pm 20\%$. The machine is planned to be used to help achieve the stringent quality control needed for the foils of the STAR Forward GEM Tracker upgrade and to assist in the development of GEMs with other hole geometries (besides double-conical) at MIT.

Bibliography

[1] F. Sauli. GEM: A new concept for electron amplification in gas detectors. *Nucl. Instrum. Methods*, A 386:531–534, 1997.

[2] The COMPASS Collaboration. COMPASS: A proposal for a COmmon Muon and Proton Apparatus for Structure and Spectroscopy. CERN/SPSLC 96-14, SPSC/P 297, Mar. 1996.

[3] F. H. Heinsius. Spin physics and the COMPASS experiment at CERN. *AIP Conf. Proc.*, 610:1007–1011, 2002.

[4] B. Ketzer et al. Triple GEM tracking detectors for COMPASS. *IEEE Trans. Nucl. Sci.*, 49:2403–2410, 2002.

[5] B. Ketzer et al. Performance of triple GEM tracking detectors in the COMPASS experiment. *Nucl. Instrum. Methods*, A 535:314–318, 2004.

[6] K.H. Ackermann et al. STAR detector overview. *Nucl. Instrum. Methods*, A 499:624–632, 2003.

[7] J.W. Harris et al. The STAR experiment at the relativistic heavy ion collider. *Nucl. Phys.*, A 556:277–286, 1994.

[8] B. Surrow. Exploring the spin structure and dynamics of the proton in high-energy polarized pp collisions at RHIC. Presentation at MIT Graduate Student Open House, Mar. 2005.

[9] R.-D. Heurer, D. Miller, F. Richard, and P. Zerwas, editors. *TESLA Technical Design Report, Part III: Physics at an e^+e^- Linear Collider.* DESY, Hamburg, Germany, Mar. 2001.

[10] T. Behnke, S. Bertolucci, R.-D. Heurer, and R. Settles, editors. *TESLA Technical Design Report, Part IV: A Detector for TESLA.* DESY, Hamburg, Germany, Mar. 2001.

[11] P. Grannis et al. Understanding matter, energy, space, and time: The case for the linear collider. `http://sbhepnt.physics.sunysb.edu/~grannis/ilcsc/lc_icfa_v6.3.pdf`, April 2003.

[12] S. Roth. Charge transfer of GEM structures in high magnetic fields. *Nucl. Instrum. Methods.*, A 535:330–333, 2004.

[13] M. Danielsson et al. Novel gaseous detectors for medical imaging. *Nucl. Instrum. Methods*, A 518:406–410, 2004.

[14] E. Tsyganov et al. Triple GEM structure for medical imaging. In *Nuclear Science Symposium Conference Record*, volume 2, pages 1163–1166. IEEE, Nov. 2002.

[15] H. Bradt and R.A. Remillard. An all-sky advanced x-ray monitor (AXM) mission. In R. Giacconi, L. Stella, and S. Serio, editors, *Proceedings of X-ray Astronomy 2000*, PASP Conference Series, Palermo, Italy, Sept. 2000.

[16] P. S. Barbeau et al. A first mass production of gas electron multipliers. *Nucl. Instrum. Methods*, A 515:439–445, 2003.

[17] B. Azmoun, G. Karagiogi, and C. Woody. A comparative study of GEM foils from different manufacturers. Technical report, BNL, 2004. PHENIX Technical Note.

[18] J. Benlloch et al. Further developments and beam tests of the gas electron multiplier (GEM). *Nucl. Instrum. Methods*, A 419:410–417, 1998.

[19] J. Benlloch et al. Development of the gas electron multiplier (GEM). *IEEE Trans. Nucl. Sci.*, 45:234–243, 1998.

[20] O. Bouianov et al. Foil geometry effects on GEM characteristics. *Nucl. Instrum. Methods*, A 458:698–709, 2001.

[21] O. Bouianov et al. Progress in GEM simulation. *Nucl. Instrum. Methods*, A 450:277–287, 2000.

[22] R. Bouclier et al. The gas electron multiplier (GEM). *IEEE Trans. Nucl. Sci.*, 44:646–650, 1997.

[23] S. Bachmann et al. Charge amplification and transfer processes in the gas electron multiplier. *Nucl. Instrum. Methods*, A 438:376–408, 1999.

[24] A. Sharma. 3D simulation of charge transfer in a gas electron multiplier (GEM) and comparison to experiment. *Nucl. Instrum. Methods*, A 454:267–271, 2000.

[25] W. Bonivento et al. A complete simulation of a triple-GEM detector. *IEEE Trans. Nucl. Sci.*, 49:1638–1643, 2002.

[26] U. Becker. Private communication, April 2005.

[27] W. Blum and L. Rolandi. *Particle Detection with Drift Chambers.* Springer-Verlag, New York, 1994.

[28] U. Becker. Unpublished data, Oct. 2004.

[29] O. Bouianov. Triple GEM simulation. Technical report, MIT LNS, 2004.

[30] The Mathworks, Inc., Natick, MA. *MATLAB Function Reference Volume 1:A–E*, 2004.

[31] U. Becker, S. Hertel, and B. Tamm. Automatic scanner for new GEMs and first results. In preparation, 2005.

[32] S. Hertel. Unpublished data, April 2005.